Department of Physics
University of Oxford

Linear Paul trap design for high-fidelity, scalable quantum information processing

Sarah R. Woodrow

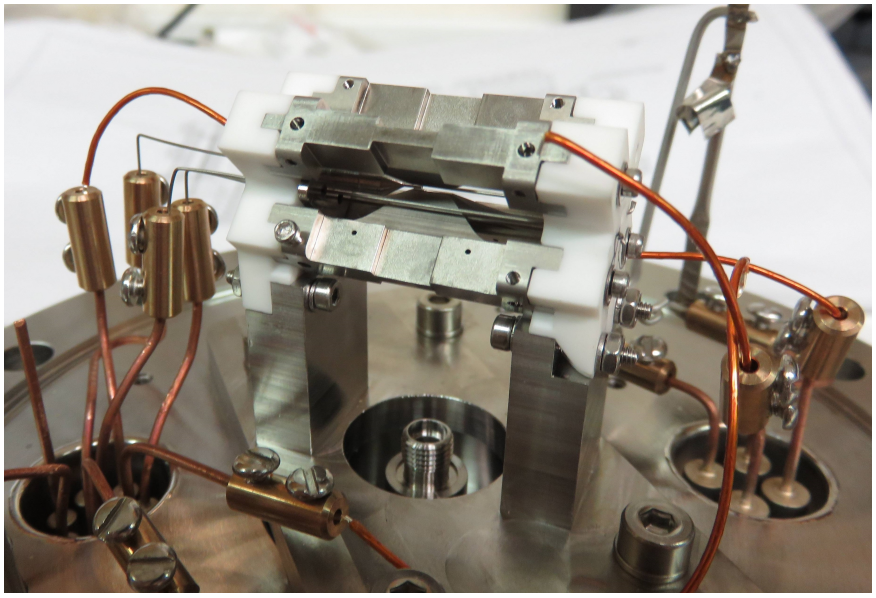

A thesis submitted for the degree of
Master of Science by Research

Wadham College
Trinity Term, 2015

Abstract

Linear Paul trap design for high-fidelity, scalable quantum information processing

Sarah R. Woodrow

A thesis submitted for the degree of Master of Science by Research

Trinity Term 2015

Wadham College, Oxford

We have designed and built a new linear Paul trap to expand our capability for carrying out high-fidelity quantum logic. We have identified some key limitations of our existing trap: the presence of a magnetic field gradient of $0.6\,\mathrm{mG\,\mu m^{-1}}$, which limits the fidelity of Bell state preparation; a high axial micromotion amplitude, which limits the fidelity of operations on linear ion crystals; and a small numerical aperture in the imaging system, which restricts the collection efficiency and thus the performance of remote entanglement experiments.

We have carried out theoretical investigations into axial ion micromotion, including a full analysis of ion motion, using numerical simulations to understand the impact of electrode geometry. We have considered the effect of ion micromotion on the excitation spectrum, and how the micromotion sidebands can be used to selectively address ions within a linear crystal.

Based on this work, electrode design parameters have been selected for the new trap to prioritise sideband addressing while maintaining the most useful properties of the existing design. We have redesigned the mechanical structure of the trap, carefully considering manufacturing limitations, to minimise the magnetic field gradient, increase the numerical aperture to 0.6 and accurately align the electrodes. Additionally, we have considered methods of characterising the trap performance to assess how well the design criteria have been met.

Acknowledgements

I am extremely grateful to my supervisor Dr. David Lucas for giving me the opportunity to join his group. His support and guidance have been absolutely invaluable throughout, and he always has words of kindness and encouragement to offer. I am also very grateful to Dr. Alastair Sinclair, my co-supervisor at NPL, for everything he has done for me.

I am equally indebted to Dr. Chris Ballance, whose enthusiasm for two-qubit gates has been great motivation in times of tedium and frustration. He has taught me more than I ever knew I wanted to know about trapping calcium ions, and has been a pleasure to work with. My sincere thanks also go to Keshav Thirumalai for all his help, and for designing the vacuum system without which the trap would be useless. He has also worked extremely hard on cleaning, polishing and assembling all the parts for the new trap (and associated vacuum system etc.) while I have been writing up.

Many thanks to the rest of the ion trap crew: Vera Schäfer, Dr. Thomas Harty, Martin Sepiol, Jamie Tarlton, Diana Prado Lopes Aude Craik, Hugo Janacek, Dr. Norbert Linke, Prof. Andrew Steane and Prof. Derek Stacey. It's been an absolute pleasure working with all of you.

Outside of the world of physics, I owe a great debt of thanks to Emma Lewis, who has always provided a listening ear, invaluable advice and infinite cups of tea, and also to Dr. Caroline Mawson for always managing to make time for me, and her superhuman ability to track down the right people at the right time. I would also like to thank Dr. Rachel Hardwick for her help and support.

I gratefully acknowledge funding from the National Physical Laboratory and EPSRC, who have given me the opportunity to undertake this research via an iCASE studentship.

Finally, I am forever grateful to my parents, my siblings Ruth and Simon, and Patrick for their abundant love, support and kindness. Thank you.

Contents

1

Introduction

Despite the huge successes of classical computing, there are many problems that are intractable on a classical Turing machine as their difficulty scales exponentially with problem size. In 1985 Deutsch proposed a 'universal quantum computer' [7] constructed from two-state quantum systems, which would possess properties not reproducible by any classical Turing machine. Many algorithms have been designed which would exploit these properties to solve important problems; an important example is Shor's algorithm, which allows efficient factorisation of large numbers, a problem whose difficulty underpins many current public-key cryptography schemes. Trapped ions have thus far proven to be one of the most promising platforms for quantum computing. Each of the DiVincenzo criteria has been met individually in systems based on trapped atomic ions, with the qubits stored in internal atomic energy levels.

Our group currently uses a macroscopic linear blade Paul trap, referred to as 'mark 2 linear trap' (see section 2.1 for trap geometry), to carry out quantum computing experiments. In particular we have implemented a two-qubit entangling gate using $^{43}Ca^{+}$ ions, achieving a maximum gate fidelity of $99.9(1)\%$, with qubit states in the $4S_{1/2}$ ground level [2]. In the future we plan to further improve upon this fidelity, as well as implementing entangling gates between $^{43}Ca^{+}$ and $^{88}Sr^{+}$ (building on our implementation of a mixed-species $^{43}Ca^{+}$-$^{40}Ca^{+}$ gate [3]), and between two $^{43}Ca^{+}$ ions in separate traps using photonic

interfaces [9]. We also plan to carry out single-ion addressing using axial micromotion sidebands, as described in section 1.1.1.

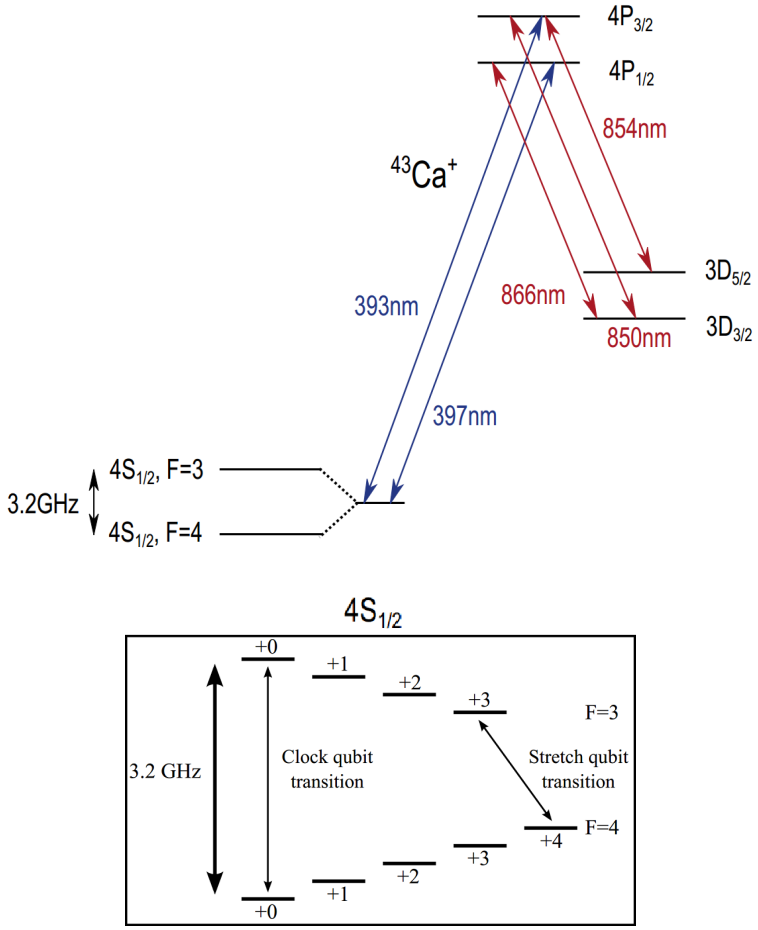

Figure 1.1: Level diagram for $^{43}Ca^{+}$, including detail of the $4S_{1/2}$ ground level with the two qubits we use labelled. [4]

1.1 Motivation for a new trap

There are several issues with our existing trap which limit our ability to carry out high-fidelity experiments. We have designed a new trap, referred to as 'mark 3 linear trap', to address these issues while maintaining the most useful properties of the current design. In particular, the mark 2 linear trap has a low heating rate (1 quantum/s), which is important to avoid decoherence in the motional degree of freedom used to implement gates.

1.1.1 Axial micromotion

One of the primary reasons for changing the trap design is to reduce the amplitude of the ions' axial micromotion. Micromotion introduces a Doppler effect, altering the excitation spectrum by adding Doppler sidebands and reducing the carrier amplitude, illustrated in figure 1.2 (see section 2.2.4 for a full discussion). Axial micromotion results from the quadratic form of the RF trapping potential along the trap axis, driving an oscillation at the trap RF frequency Ω. The resulting Doppler sidebands are spaced at $\pm n\Omega$. The amplitude of this oscillation, and hence the form of the excitation spectrum, varies along the trap axis.

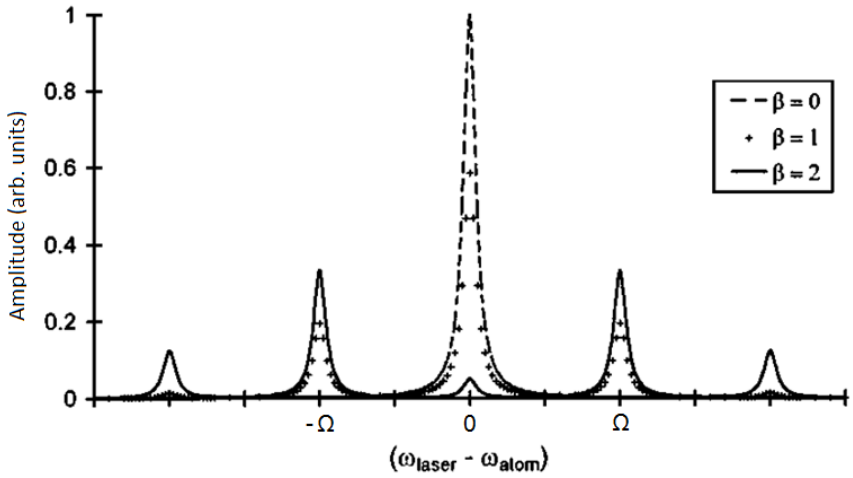

Figure 1.2: Effect of axial micromotion on the excitation spectrum. $\beta = 0$ represents zero micromotion, such as for an ion at the trap centre, with increasing values of β corresponding to a larger micromotion amplitude. Reproduced from [5] figure 2b for reference only.

We wish to carry out experiments with large ion crystals (up to 10 ions), and so we require a moderate level of consistency in the excitation spectra for ions along the crystal (ideally a deviation of $\lesssim 3\%$ in the carrier amplitude). Such experiments are impossible in the current trap due to a large micromotion amplitude; for a two-ion crystal at $\omega_z = 2\,\mathrm{MHz}, \omega_r = 4.5\,\mathrm{MHz}$ the ions are displaced by $3.5\,\mu\mathrm{m}$ along the axis, and subsequently the carrier amplitude is reduced by 20% compared to the carrier amplitude for an ion at the trap centre.

We also wish to utilise the axial micromotion to allow addressing of individual ions within linear crystals. Consider a two-ion crystal consisting of ions A and B, where ion A is at the micromotion null ($x = y = z = 0$) and ion B is displaced along $\hat{\mathbf{z}}$ ($x = y = 0$). For a laser field at frequency ω_l, the excitation spectrum of ion A will have only a single peak at ω_l, whereas the excitation spectrum of ion B will consist of a carrier at ω_l and micromotion sidebands at $\omega_l \pm n\Omega$, where Ω is the trap RF frequency. By detuning the laser to, for example, $\omega_l + \Omega$, we can perform operations only on ion B while the laser field illuminates both ions. To enable this addressing to be effective we require a large micromotion amplitude; the amplitude of the first micromotion sideband for ion B must be $\gtrsim 10\%$ of the carrier for ion A. This keeps errors from off-resonant excitation of the carrier comparable to, or smaller than, errors from photon scattering.

In practice, the configuration described above is impractical for combining single- and multi-ion operations. Due to the asymmetric positioning ions A and B have different carrier amplitudes and therefore different Rabi frequencies. Since the interaction Hamiltonian depends on Rabi frequency for any qubit manipulation it is impossible to perform the same operation on both ions with high fidelity. Instead, we position ions A and B symmetrically about the centre of the trap as in figure 1.3. Operations on the carrier therefore affect both ions identically, while operations on the first micromotion sideband take effect with opposite phase. Table 1.1 outlines a scheme which could be used to selectively apply a π pulse to ion B using this configuration. One could imagine that this could be extended to greater numbers of ions by choosing the correct combination of operations and phases such that e.g. all ions in the crystal experience an operation of $2n\pi$ ($n = 0, \pm 1, \pm 2 \ldots$), except for the ion being addressed.

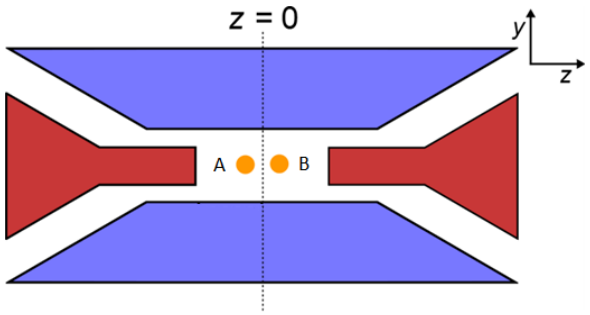

Figure 1.3: Linear two-ion crystal along the trap axis, with ions A and B equally spaced about the trap centre. This configuration allows use of axial micromotion sidebands to individually address ions, without compromising the fidelity of multi-ion operations.

Laser tuned to	Operation	Effect on A	Effect on B
Carrier	$+\pi/2$	$+\pi/2$	$+\pi/2$
1st micromotion sideband	$+\pi/2$	$-\pi/2$	$+\pi/2$
		0	$+\pi$

Table 1.1: Example scheme to selectively apply a π pulse to ion B while leaving the state of ion A unchanged, using axial micromotion sideband addressing. The configuration of ions in the trap is shown in figure 1.3.

1.1.2 Internal magnetic field gradient

In the mark 2 linear trap we observe a magnetic field gradient along the trap axis of approximately $0.6\,\mathrm{mG\,\mu m^{-1}}$ leading to a non-negligible change in the qubit frequency splitting (shown in figure 1.4) due to the Zeeman effect. This limits the fidelity of quantum operations on ions in a linear crystal.

In our current experiments we have implemented the light-shift ('wobble') gate, a geometric phase gate which entangles the internal states of the two ions by use of a spin-dependent force (described in detail in [4]). This gate mechanism uses a pair of Raman beams with a frequency difference close to a motional mode, with a polarisation chosen such that the coupling is spin-dependent, to produce the required force. Since this uses the spin properties of the qubit states rather than the energy levels, it is independent of the qubit frequency and therefore of the magnetic field experienced by the ions. The error in the gate operation is therefore unaffected by the magnetic field gradient in our trap. However with

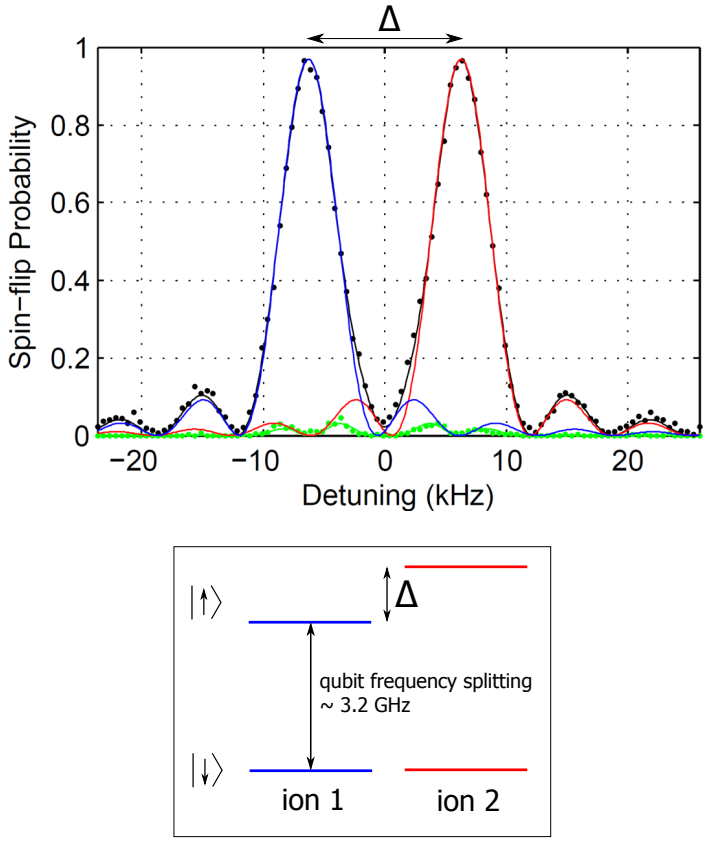

Figure 1.4: Probability of spin-flip of a single ion (ion 1 in blue, ion 2 in red) for two $^{43}Ca^{+}$ ions in a linear crystal in the existing trap, spaced $8.975\,\mu m$ apart with an axial trap frequency of $475.9(1)\,kHz$. The green data shows the probability for a spin-flip of both ions. As indicated in the level diagram, Δ indicates the difference in the qubit frequency splitting for ion 1 and ion 2. Here we show only the relevant stretch qubit states $4S_{1/2}^{3,+3}$ ($|\uparrow\rangle$) and $4S_{1/2}^{4,+4}$ ($|\downarrow\rangle$). Δ is comparable to the Rabi frequency, and is caused by a magnetic field gradient of approximately $0.6\,mG\,\mu m^{-1}$ along the trap axis. (Plot courtesy of C.J. Ballance)

this mechanism single-qubit rotations are also required to create a Bell state. The light-shift gate introduces a spin-dependent phase shift in the system state, which itself cannot be directly measured. Only by embedding the gate between a pair of $\pi/2$ pulses, or in a spin-echo sequence, do we generate the desired Bell state. Since these single-qubit operations are magnetic field dependent, the Bell state fidelity is limited by the magnetic field gradient. In addition, we plan to implement the Mølmer-Sørenson gate, which relies on coupling based on the qubit state energy levels and is therefore magnetic field dependent.

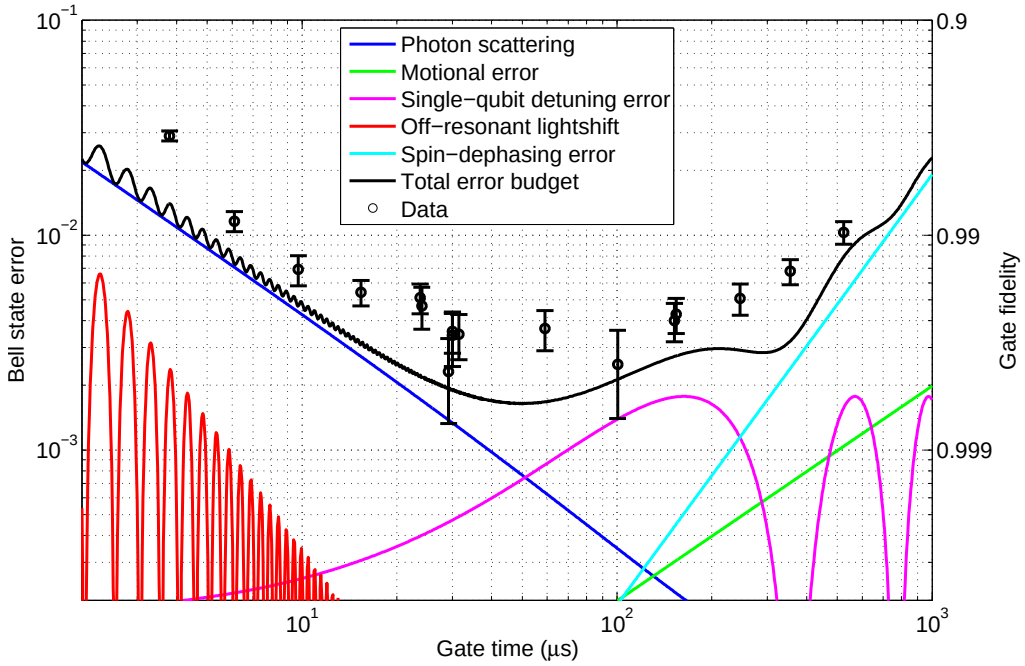

Figure 1.5: Measured Bell state fidelity, showing error contributions from different sources. The magenta line shows the single-qubit detuning error, caused by the magnetic field gradient discussed in section 1.1.2. Eliminating this error could significantly increase the Bell state fidelity, particularly for gate times between 50 µs and 200 µs. (Plot courtesy of C.J. Ballance)

The magnetic field gradient within the trap is believed to originate from the electrodes; they have become magnetised during the machining process. It is well-documented (e.g. [1]) that work hardening of non-magnetic (e.g. 300-series) steels during machining can lead to straining of the atomic lattice structure, changing the crystal grain structure from the non-magnetic austenitic to the magnetic martensite. This happens easily in 304, a standard non-magnetic grade of steel which we believe was used in the mark 2 linear trap, whereas 316 steel is more resistant to magnetisation as a higher nickel content stabilises the austenitic crystal structure.

In the mark 3 linear trap we aim to minimise magnetisation by careful selection of the trap material and manufacturing methods. We plan to use 316LN, a grade of non-magnetic stainless steel which has significant resistance to crystal grain structure changes, and anneal the material before machining to eliminate

any undesirable magnetic fields. Electrical discharge machining (EDM) will be used; this maximises the machining accuracy and we hope that it will reduce the strain on the lattice structure compared to conventional cutting techniques.

1.1.3 Numerical aperture (NA) of imaging system

A freely scalable quantum computing architecture requires a remote entangling link. We plan to implement this by linking together two multi-ion traps using a photonic interconnect, as demonstrated by Hucul et al. [9]. We wish to generate an entangled Bell state with two $^{43}Ca^{+}$ ions in separate traps. In the proposed mechanism, each ion is excited to an upper state and subsequently decays by emitting a photon which is entangled with its internal state. A Bell state measurement is performed on the emitted photons to generate a heralded entangled state.

The success of this two-qubit remote entanglement mechanism relies on collecting the emitted photons, and hence the success rate is proportional to NA^4. The existing imaging system has a numerical aperture of $\mathrm{NA} \simeq 0.2$, which would severely limit the performance of remote entanglement experiments. We will use an objective lens with $\mathrm{NA} = 0.6$, thereby increasing the probability of success by $\mathcal{O}(10^2)$.

2

Linear Paul trap theory

2.1 Trap geometry

The linear Paul trap uses a static quadrupole electric field along the axial direction $\hat{\mathbf{z}}$ (see figure 2.1 for coordinate definitions) to confine the ions axially. This field is provided by applying a potential V_{dc} to the 'endcap' electrodes, shown in red in figure 2.1. However, from Poisson's equation $\nabla \cdot \mathbf{E} = 0$, we find that a field cannot be confining in all three dimensions. This quadrupole field has a saddle point at the trap origin, resulting in an anti-confining force in one radial direction. Radial confinement is provided by a high-frequency RF potential applied to two pairs of 'blade' electrodes (shown in yellow and blue in figure 2.1), generating a 2D quadrupole field in the radial plane. We drive the blade electrodes asymmetrically, connecting one pair to ground and the other pair to a single RF source with peak amplitude V_{ac} and frequency Ω. For a typical 2-ion linear crystal with axial and radial frequencies $\omega_z = 2\pi \cdot 2\,\mathrm{MHz}$, $\omega_r = 2\pi \cdot 4\,\mathrm{MHz}$ in the mark 2 linear trap we have $V_{dc} \simeq 150\,\mathrm{V}, V_{ac} \simeq 800\,\mathrm{V}$. The radial trap frequency must be higher than the axial frequency to maintain a linear crystal of ions along the axis; this is discussed in more detail in section 2.3.

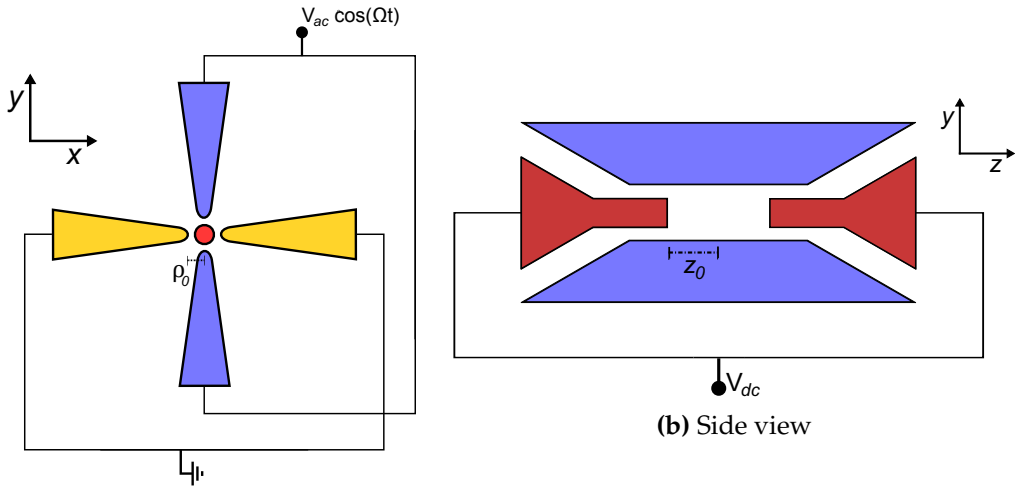

(a) End view

(b) Side view

Figure 2.1: Linear Paul trap electrode geometry, showing the asymmetric RF drive. We define the trap centre as $x = y = z = 0$. For a typical 2-ion crystal with axial and radial frequencies $\omega_z = 2\pi \cdot 2\,\mathrm{MHz}$, $\omega_r = 2\pi \cdot 4\,\mathrm{MHz}$ in our existing trap we have $V_{dc} \simeq 150\,\mathrm{V}, V_{ac} \simeq 800\,\mathrm{V}$.

2.2 Axial ion micromotion

Theoretical calculations of ion motion in a Paul trap are covered well in many texts (e.g. [8] section 2.1). However, these typically make broad assumptions to focus primarily on trap stability conditions. In particular, the standard treatment assumes that the RF potential applied to the trap blades affects only the motion in the radial plane, and neglects any effect on the motion along the trap axis. In fact, it is this potential that leads to the axial micromotion we are concerned with. This section aims to carry out analysis of the ion's motion using the standard Mathieu equation approach, while including effects that lead to axial micromotion.

2.2.1 Electric potential

An RF voltage applied to the blades as shown in figure 2.1, with angular frequency Ω and peak amplitude V_{ac}, produces an oscillating 2D quadrupole field in the radial plane with amplitude Q_r^{ac}. We define

$$Q_r^{ac} = \frac{\alpha_r^{ac} V_{ac}}{\rho_0^2} \tag{2.1}$$

where ρ_0 is the distance from the trap axis to the nearest blade electrode surface, and α_r^{ac} is a geometrical factor which describes the blade electrode geometry.

We also consider the effect of the the RF voltage along the trap axis. Electrostatic fields sum linearly and so we can gain an understanding of the fields by considering the endcap electrodes to be grounded. With a non-zero potential along the axis at the centre of the trap due to the RF voltage on the blades, this results in a 1D quadratic potential along the trap axis, oscillating at Ω, with amplitude Q_z^{ac}. We define

$$Q_z^{ac} = \frac{\alpha_z^{ac} V_{ac}}{z_0^2} \tag{2.2}$$

where z_0 is the distance from the trap centre to the endcap electrode surface, and α_z^{ac} is a geometrical factor.

A DC voltage V_{dc} applied to the endcaps as shown in figure 2.1 produces a DC quadrupole field of amplitude Q_z^{dc}, which provides confinement along the trap axis. We define

$$Q_z^{dc} = \frac{\alpha_z^{dc} V_{dc}}{z_0^2} \tag{2.3}$$

where α_z^{dc} is a geometrical factor. We can consider this as a parameter which describes the shielding of the endcap potential due to the presence of the RF electrodes.

The resulting potential is:

$$V = Q_z^{dc}\left[z^2 - \left(\frac{x^2+y^2}{2}\right)\right] + \left[Q_r^{ac}\left(x^2-y^2\right) - Q_z^{ac} z^2 + \frac{1}{2}V_{ac}\right]\cos(\Omega t) \tag{2.4}$$

2.2.1.1 Asymmetric drive

In the potential above, the $Q_z^{ac} z^2$ and $\frac{1}{2} V_{ac}$ terms result from the asymmetric drive shown in figure 2.1. While the second term is a homogeneous potential that has no impact on the trapping fields, the z^2 dependence of the first term leads to the axial micromotion studied here. We can alternatively consider applying the RF drive symmetrically, i.e. with one pair of blades at $+V_{ac}\cos(\Omega t)$ and the other at $-V_{ac}\cos(\Omega t)$, which would eliminate these terms (and therefore the resulting axial micromotion) entirely.

The use of two RF sources applied to different electrodes introduces significant technical difficulties, however, since any phase difference between the two sources introduces radial micromotion as described in [5]. While steps can be taken to minimise phase differences (e.g. driving both sources from a common resonator), this is a technically challenging and time-consuming process. Differential RF noise between the two sources, which is difficult to eliminate, also causes radial mode heating leading to decoherence. In the case of our experiment a consistent, well-known level of axial micromotion arising from the asymmetric drive is tolerable, and is preferable to compromising our low heating rate. In addition, we are capable of reducing the axial micromotion to acceptable levels by changing the trap geometry (see section 3).

2.2.1.2 Radial asymmetry

Since the trap geometry is symmetric in $\hat{\mathbf{x}}$ and $\hat{\mathbf{y}}$ one would expect the motion and parameters to share the same symmetry, becoming radially symmetric near the trap centre. However, the RF drive scheme specified in section 2.1 leads to asymmetries between parameters in $\hat{\mathbf{x}}$ and $\hat{\mathbf{y}}$. Instead of equation 2.1, we should strictly define

$$Q_x^{ac} = \frac{\alpha_x^{ac} V_{ac}}{\rho_0^2} \qquad\qquad Q_y^{ac} = \frac{\alpha_y^{ac} V_{ac}}{\rho_0^2} \tag{2.5}$$

where the definitions from equation 2.1 apply, and $\alpha_x^{ac} \neq \alpha_y^{ac}$ are the geometrical factors for $\hat{\mathbf{x}}$ and $\hat{\mathbf{y}}$ respectively. The resulting potential in equation 2.4 would therefore be modified accordingly. However, one finds that this asymmetry is small (typically $\sim$ 1-2%), and so here we will neglect this effect by defining

$$\alpha_r^{ac} = \frac{\alpha_x^{ac} + \alpha_y^{ac}}{2} \tag{2.6}$$

such that equations 2.1 and 2.4 hold.

2.2.2 Equations of motion

For an ionised particle with charge $+Ze$ and mass m moving in this potential the resultant force is given by $\mathbf{F} = -Ze\nabla V$. The motion is separable and so we carry out the analysis in $\hat{\mathbf{x}}$, $\hat{\mathbf{y}}$ and $\hat{\mathbf{z}}$ independently.

The equations of motion are given by:

$$\frac{\mathrm{d}^2 x}{\mathrm{d}t^2} = \frac{Ze}{m}\left[Q_z^{dc} - 2Q_r^{ac}\cos(\Omega t)\right] x \tag{2.7}$$

$$\frac{\mathrm{d}^2 y}{\mathrm{d}t^2} = \frac{Ze}{m}\left[Q_z^{dc} + 2Q_r^{ac}\cos(\Omega t)\right] y \tag{2.8}$$

$$\frac{\mathrm{d}^2 z}{\mathrm{d}t^2} = \frac{2Ze}{m}\left[-Q_z^{dc} + Q_z^{ac}\cos(\Omega t)\right] z \tag{2.9}$$

The following treatment is carried out for the equation of motion in each dimension. Here we outline the procedure for $\hat{\mathbf{z}}$, and quote the results for $\hat{\mathbf{x}}$ and $\hat{\mathbf{y}}$.

Substitution of $\Omega t = 2\tau$ results in

$$\frac{\mathrm{d}^2 z}{\mathrm{d}\tau^2} = -\frac{8Ze}{m\Omega^2}\left[Q_z^{dc} - Q_z^{ac}\cos(2\tau)\right] z \tag{2.10}$$

which is in the form of a standard Mathieu equation

$$\frac{\mathrm{d}^2 z}{\mathrm{d}\tau^2} + \left[a_z - 2q_z \cos(2\tau)\right] z = 0 \tag{2.11}$$

We find that the equation of motion in each direction can be expressed in this form, giving the Mathieu parameters

$$\begin{aligned} a_x &= -\frac{4ZeQ_z^{dc}}{m\Omega^2} & q_x &= -\frac{4ZeQ_r^{ac}}{m\Omega^2} \\ a_y &= -\frac{4ZeQ_z^{dc}}{m\Omega^2} & q_y &= +\frac{4ZeQ_r^{ac}}{m\Omega^2} \\ a_z &= +\frac{8ZeQ_z^{dc}}{m\Omega^2} & q_z &= +\frac{4ZeQ_z^{ac}}{m\Omega^2} \end{aligned} \tag{2.12}$$

Analytical approximate solutions to the Mathieu equation are well-known, and we find there are several conditions required for stable trapping. These are discussed elsewhere (e.g. [8] section 2.1); here we consider $|q_i| \lesssim 0.5$ and $|a_i| < \frac{q_i^2}{2}$ for $i = x, y$ to be sufficient. These requirements can be interpreted physically: the first specifies a maximum amplitude of the oscillatory RF force at Ω to ensure a stable orbit; the second states that the confining RF force must exceed the anti-confining DC force. Note that $\sum_{i=x,y,z} a_i = 0$; this is a consequence of Laplace's equation. $a_x, a_y < 0$ is a statement of the anti-confining nature of the DC force in the radial direction.

2.2.3 Secular motion and micromotion

We use the pseudo-potential model to find simplified approximate solutions to the Mathieu equations. The calculations are covered elsewhere (e.g. [8] section 2.1.2) and so we will quote the assumptions and results here.

We assume that the particle position, $\mathbf{r} = r_x\hat{\mathbf{x}} + r_y\hat{\mathbf{y}} + r_z\hat{\mathbf{z}}$, can be separated into components

$$\mathbf{r} = \bar{\mathbf{r}} + \boldsymbol{\delta} \tag{2.13}$$

where $\bar{\mathbf{r}}$ is the average ion displacement over a period of RF, representing the secular motion, and $\boldsymbol{\delta}$ is a displacement of small amplitude from this average, representing the micromotion.

Under the assumptions that $\boldsymbol{\delta} \ll \bar{\mathbf{r}}$ and $\Omega/\omega_i \gg 1$, where $i = x, y, z$ and ω_i is the secular motional frequency, the analysis leads to

$$\delta_i = -\frac{q_i \bar{r}_i}{2} \cos(2\tau) \tag{2.14}$$

i.e. the micromotion is an oscillation about the ion's average position with frequency Ω and amplitude $d_i = \frac{q_i \bar{r}_i}{2}$. Since we consider a linear crystal of ions, where all ions lie on $x = y = 0$ with displacement along $\hat{\mathbf{z}}$ only, the ions have micromotion only along the trap axis $\hat{\mathbf{z}}$ with $d_x = d_y = 0$. We therefore consider only

$$d_z = \frac{q_z \bar{z}}{2} \tag{2.15}$$

We also find the secular motional frequencies:

$$\omega_i = \frac{\Omega}{2} \sqrt{\frac{q_i^2}{2} + a_i} \tag{2.16}$$

As described in section 2.2.1.2, we assume radial symmetry. Hence we define radial parameters

$$q_r = \frac{|q_x| + |q_y|}{2} = \frac{4ZeQ_r^{ac}}{m\Omega^2}; \quad a_r = \frac{|a_x| + |a_y|}{2} = \frac{4ZeQ_z^{dc}}{m\Omega^2}; \quad \omega_r = \frac{\Omega}{2}\sqrt{\frac{q_r^2}{2} - a_r} \tag{2.17}$$

which will be used from this point forward.

In the axial direction, $\hat{\mathbf{z}}$, the RF potential on the blades has only a small effect on the secular motion. We find that $q_z \ll a_z$ and hence we can approximate

$$\omega_z \simeq \frac{\Omega}{2}\sqrt{a_z} = \sqrt{\frac{2ZeQ_z^{dc}}{m}} \tag{2.18}$$

In practice we wish to specify: the number of trapped ions, N; trap motional frequencies ω_z and ω_r; and the RF drive frequency Ω. Note that care must be taken to select values of ω_z and ω_r which allow confinement of a stable linear N-ion crystal (see section 2.3). For a given trap geometry we know z_0 and ρ_0; α_r^{ac}, α_z^{ac} and α_z^{dc} are found from the numerical simulations discussed in section 3.

From equations 2.12, 2.17 and 2.18 we can write

$$\omega_r = \frac{\Omega}{2}\sqrt{\frac{q_r^2}{2} - \frac{2\omega_z^2}{\Omega^2}} \tag{2.19}$$

and hence we find

$$q_r = \frac{\sqrt{8\omega_r^2 + 4\omega_z^2}}{\Omega} \tag{2.20}$$

Note this is independent of trap geometry.

Using equations 2.1, 2.2, 2.12 and 2.17 we can rearrange to find

$$q_r = \frac{4Ze\alpha_r^{ac}V_{ac}}{\Omega^2 m\rho_0^2} \qquad\qquad q_z = \frac{4Ze\alpha_z^{ac}V_{ac}}{\Omega^2 m z_0^2} \tag{2.21}$$

and hence

$$q_z = q_r\frac{\alpha_z^{ac}}{\alpha_r^{ac}}\left(\frac{\rho_0}{z_0}\right)^2 \tag{2.22}$$

From this we can calculate the axial micromotion amplitude in equation 2.15 directly.

We can also use equations 2.3 and 2.18 to find that

$$V_{dc} = \frac{\omega_z^2 m z_0^2}{2Ze\alpha_z^{dc}} \tag{2.23}$$

and similarly, using equations 2.1 and 2.12, we can write

$$V_{ac} = \frac{q_r m\Omega^2\rho_0^2}{4Ze\alpha_r^{ac}} \tag{2.24}$$

This allows us to find the trap voltages necessary to achieve a given trap strength.

2.2.4 Spectral micromotion sidebands

Axial micromotion introduces a Doppler shift which can significantly alter the excitation spectrum of the ions' atomic transitions. This is analysed elsewhere e.g. by Berkeland et al. [5] (section III), and we will use their assumptions and results.

The ion is excited by a laser field with amplitude $\mathbf{E}_0 \in \mathbb{R}$, frequency ω_l, phase ϕ_l and wave vector $\mathbf{k}$. In the rest frame of an ion undergoing micromotion, the laser field can be expressed with a Bessel function expansion as

$$\mathbf{E}(t) = \mathbb{R}\left\{\mathbf{E}_0 e^{i\mathbf{k}\cdot\bar{\mathbf{r}}} \sum_{n=-\infty}^{\infty} J_n(\beta)\exp\left[-i\omega_l t + \phi_l + in(\Omega t + \pi/2)\right]\right\} \tag{2.25}$$

where $\bar{\mathbf{r}}$ is the average ion displacement as discussed in section 2.2.3, $\beta = \mathbf{k}\cdot\mathbf{d}$ with $\mathbf{d}$ the micromotion amplitude vector, and Ω is the RF drive frequency. As discussed in section 2.2.3 the ions in a linear crystal undergo axial micromotion only and so $\mathbf{d} = d_z\hat{\mathbf{z}}$ and $\bar{\mathbf{r}} = \bar{z}$. We perform coherent qubit manipulation with a pair of Raman beams with wavelength $\lambda_{397} = 397\,\mathrm{nm}$, at $45°$ to $\hat{\mathbf{z}}$ as shown in figure 2.2, and hence we find that $\beta = (\mathbf{k_1} - \mathbf{k_2})\cdot\mathbf{d} = \sqrt{2}k_{397}d_z$, where $k_{397} = {}^{2\pi}/_{\lambda_{397}}$, $\lambda_{397} = 397\,\mathrm{nm}$.

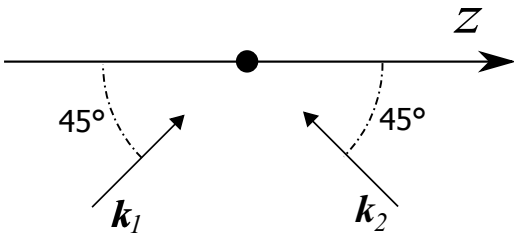

Figure 2.2: Sketch showing the configuration of $397\,\mathrm{nm}$ Raman beams used to perform coherent qubit manipulation

Note that equation 26 in [5] also contains a term dependent on ϕ_{ac}, the phase difference between the RF potentials applied to pairs of blade electrodes. For the

asymmetric RF drive described in section 2.1, with one pair of blades grounded, we have $\phi_{ac} = 0$ by definition and so we neglect this term.

The result is a frequency modulation of the laser field. The excitation spectrum (in frequency space) consists of the carrier at ω_l and sidebands at $\omega_l \pm n\Omega$ with amplitudes

$$E_n = E_{0z} J_n(\beta) \tag{2.26}$$

2.3 Stability & linear ion crystals

In section 2.2.2 we considered $|q_i| \lesssim 0.5$ and $|a_i| < \frac{q_i^2}{2}$ for $i = x, y, z$ to be sufficient conditions for stable trapping of ions. To maintain a linear ion crystal, additional requirements must be met in order to avoid resonant mixing of the transverse motional modes, which causes instabilities. This process is examined in detail by Marquet et al. [11], and here we will quote their results. We define a trap anisotropy parameter

$$\alpha = \left(\frac{\omega_z}{\omega_r}\right)^2 \tag{2.27}$$

where ω_z and ω_r are the secular axial and radial motional frequencies respectively. Figure 2 in [11] shows the values of α for which resonant mode mixing can occur; we reproduce it here as figure 2.3 for reference only. We wish to operate our trap in a regime where ion crystals are not affected by mode mixing; ideally $\alpha < \alpha_{\text{safe}}$, and we certainly require $\alpha < \alpha_{\text{crit}}$ for ion crystal stability.

As found in equation 2.15 the axial micromotion amplitude d_z for an ion confined on the axis varies linearly with ion axial equilibrium position $\bar{z}$, and hence to find the micromotion amplitude for an ion we must first know the equilibrium position. By considering potential energy of ions in the chain due to the harmonic trapping force and the inter-ion repulsion, James et al. [10]

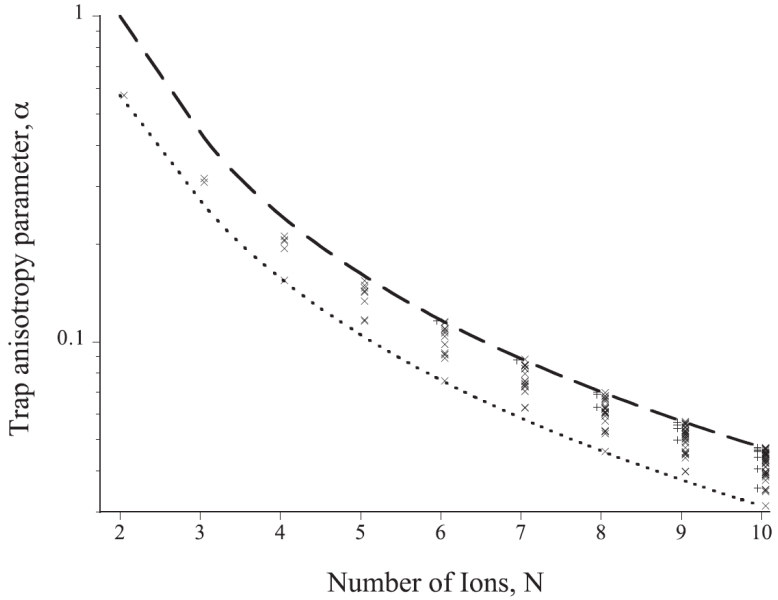

Figure 2.3: Reproduced from Marquet et al figure 2 [11] for reference only. Values of the trap anisotropy parameter α for which resonant mode mixing can occur, causing crystal instability. The crosses represent resonance conditions. The upper limiting curve represents the critical value α_{crit}, above which the linear configuration of ions becomes unstable. The lower curve represents α_{safe}, the highest value of α for which resonant mode mixing cannot occur.

calculate numerically the equilibrium positions for ions in a linear crystal. Table 2.1 shows the scaled equilibrium positions, with length scale l defined by

$$l^3 = \frac{Z^2e^2}{4\pi\epsilon_0 m\omega_z^2} \tag{2.28}$$

for an ionised particle with charge $+Ze$ and mass m, trapped with axial secular frequency ω_z, where ϵ_0 is the permittivity of free space.

N	Scaled equilibrium positions									
2					−0.62996	0.62996				
3					−1.0772	0	1.0772			
4				−1.4368	−0.45438	0.45438	1.4368			
5				−1.7429	−0.8221	0	0.8221	1.7429		
6			−2.0123	−1.1361	−0.36992	0.36992	1.1361	2.0123		
7		−2.2545	−1.4129	−0.68694	0	0.68694	1.4129	2.2545		
8	−2.4758	−1.6621	−0.96701	−0.31802	0.31802	0.96701	1.6621	2.4758		
9	−2.6803	−1.8897	−1.2195	−0.59958	0	0.59958	1.2195	1.8897	2.6803	
10	−2.8708	−2.10003	−1.4504	−0.85378	−0.2821	0.2821	0.85378	1.4504	2.10003	2.8708

Table 2.1: Reproduced from James et al. table 1 [10] for reference only. Scaled equilibrium positions of trapped ions in an N-ion linear crystal. To find the equilibrium position, multiply by the length scale $l = \left(\frac{Z^2e^2}{4\pi\epsilon_0 m\omega_z^2}\right)^{1/3}$.

2.4 Experimental parameters

Experimentally, we must set Ω, ω_z and ω_r. The RF drive is provided by a high-Q helical resonator with resonant frequency Ω. A new helical resonator will be built for use with the mark 3 linear trap, so we can therefore choose Ω, but it will be difficult to alter this once the resonator is constructed. ω_z and ω_r can easily be modified by altering the trapping voltages, and it is common to change these as necessary during trapping.

The mark 2 linear trap primarily uses $\omega_z = 2\pi \cdot 2\,\mathrm{MHz}, \omega_r = 2\pi \cdot 4\,\mathrm{MHz}$ and $\Omega = 2\pi \cdot 30\,\mathrm{MHz}$. This gives $q_r = 0.37$ and $\alpha = 0.25$, which satisfies the condition $q_r \lesssim 0.5$ for stable confinement but only allows a maximum of ~ 3 ions to be confined in a stable linear crystal (see figure 2.3). This choice of parameters has some strong advantages. It is best to maximise ω_z as far as possible since, among other reasons: higher ω_z allows for a lower $\bar{n}$ for the same temperature; heating rates scale as $\sim 1/\omega_z^2$; the Lamb-Dicke parameter η is smaller for a higher ω_z; gate operations can be performed faster with a higher ω_z since errors are due to off-resonant excitation. Note also that the required RF drive amplitude V_{ac} depends quadratically on Ω (see equation 2.24) and so it is impractical to increase Ω too far while maintaining a stable and accurate RF supply. We will therefore aim to keep these parameters roughly constant.

We consider the definition of q_r in equation 2.20. Since we have $\omega_r > \omega_z$ we generally have $8\omega_r^2 \gg \omega_z^2$ and hence we choose to approximate

$$q_r \simeq \frac{2\sqrt{2}\omega_r}{\Omega} \tag{2.29}$$

To satisfy the condition $q_r \lesssim 0.5$ we must keep $\omega_r \lesssim 2\pi \cdot 5\,\mathrm{MHz}$. To decrease α (and thereby increase N) we therefore only have the option of decreasing ω_z. To enable stable confinement of a 10-ion crystal we require $\alpha \lesssim 0.04$, and hence $\omega_z \sim 2\pi \cdot 1\,\mathrm{MHz}$. We will therefore carry out the analysis of simulations using

two sets of parameters: $\omega_z = 2\pi \cdot 2\,\mathrm{MHz}, \omega_r = 2\pi \cdot 4\,\mathrm{MHz}$ for a 2-ion crystal, and $\omega_z = 2\pi \cdot 1\,\mathrm{MHz}, \omega_r = 2\pi \cdot 5\,\mathrm{MHz}$ for N-ion crystals with $N > 2$.

3

Numerical simulations

Numerical simulations were carried out using *Charged Particle Optics* (CPO), a suite of software which uses the Boundary Element Method to calculate electrostatic fields resulting from a specified configuration of electrodes. Interface with the CPO program, as well as analysis of the results, was implemented using MATLAB.

We wish to simulate the trap geometry shown in section 2.1 with a DC potential applied to the endcaps, one pair of blades grounded (at zero potential) and an RF potential applied to the other pair of blades. There are two key facts which allow us to achieve this using simulations of electrostatic fields. Due to the linearity of Maxwell's equations we can apply a potential in turn to each electrode of interest, with all others at zero potential, and the total field then is found from a linear sum of all resulting fields. We also observe that the RF frequency $\Omega \sim 30\,\mathrm{MHz}$ is low enough to avoid any electromagnetic wave effects over the dimensions of the trap, and so we can simulate the RF field using electrostatics. We then use the equations in sections 2.2.3 and 2.2.4 to analyse the results and find the expected micromotion amplitude and the excitation spectrum described in section 2.2.4.

3.1 Simulation method

We first apply a unit potential to the endcap electrodes, with the blades at zero potential. We calculate the potential only for a small volume ($0.1 \times 0.1 \times 0.1$ mm^3) at the centre of the trap. We observe a quadratic confining potential along $\hat{\mathbf{z}}$ (with $x = y = 0$) and can fit the expected analytic form of the potential (figure 3.1). This allows us to find Q_z^{dc} and α_z^{dc} from equations 2.3 and 2.4. Specifically, for $x = y = 0$ and $V_{ac} = 0$, we have $V = Q_z^{dc} z^2$ and a quadratic fit $V = az^2 + bz + c$, hence $Q_z^{dc} = a$. Figure 3.1 shows this simulation for the existing mark 2 linear trap geometry. We notice from the form of the residuals that the simulation is not a perfect quadratic. This is partially due to infidelities in the simulation; we would expect the potential to vary smoothly, and so any sharp changes must be unphysical. We also consider the practicalities of manufacturing and assembling the trap electrodes; it is unlikely that, even with great care taken, we will be able to construct the trap geometry to better than 1% accuracy, and so the simulated $\mathcal{O}(10^{-4})$ errors from the non-quadratic nature of the potential will be negligible in comparison to misalignment errors.

We then apply a unit potential to one pair of blade electrodes, with all other electrodes grounded. We observe the expected quadratic fields along $\hat{\mathbf{x}}$ ($y = z = 0$) and $\hat{\mathbf{y}}$ ($x = z = 0$), as shown in figure 3.2, and similarly we can find $Q_x^{ac}, Q_y^{ac}, \alpha_x^{ac}$ and α_y^{ac}. Recall we have defined α_r^{ac} from equation 2.6. We also observe the potential along $\hat{\mathbf{z}}$ ($x = y = 0$), as shown in figure 3.3, to find Q_z^{ac} and α_z^{ac}. Again we note that the simulated errors from the non-quadratic nature of the potentials are negligible in comparison to the expected misalignment errors.

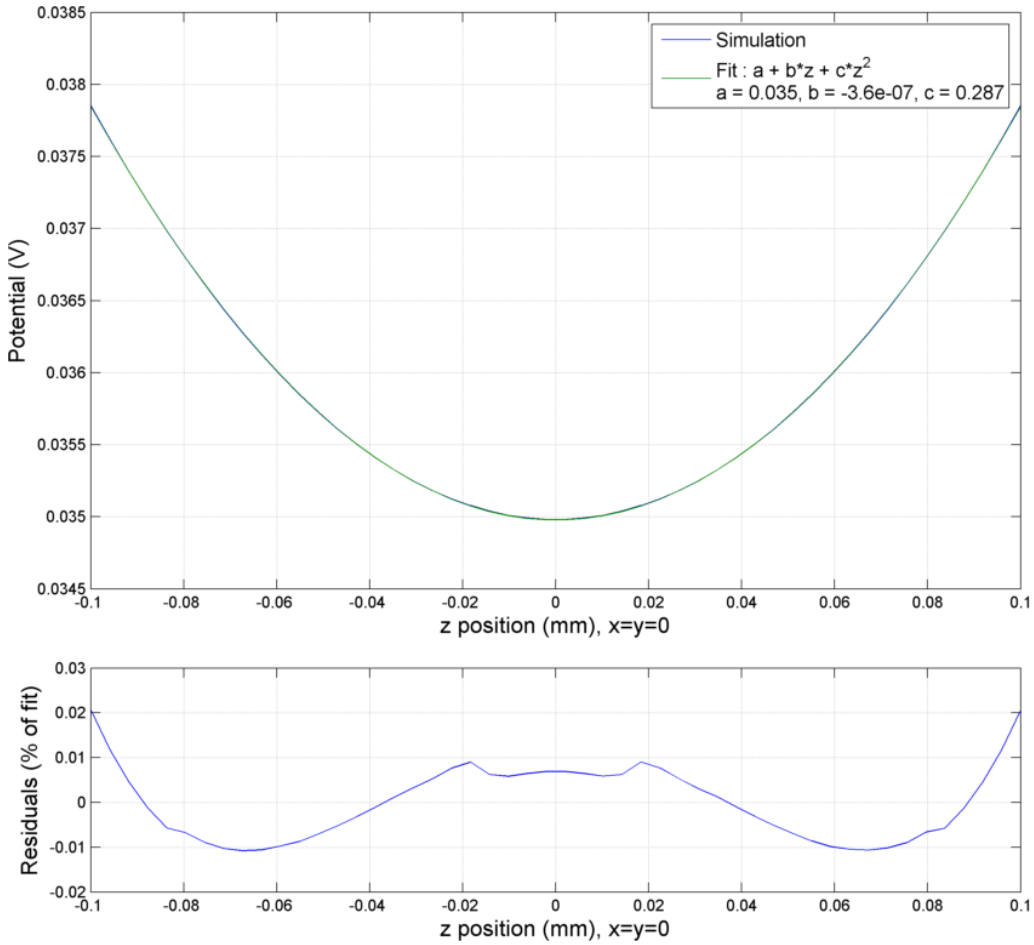

Figure 3.1: Simulated DC potential along the trap axis, $\hat{\mathbf{z}}$ ($x = y = 0$), in the existing mark 2 linear trap geometry. $1\,\mathrm{V}$ is applied to the endcap electrodes and all blade electrodes are grounded.

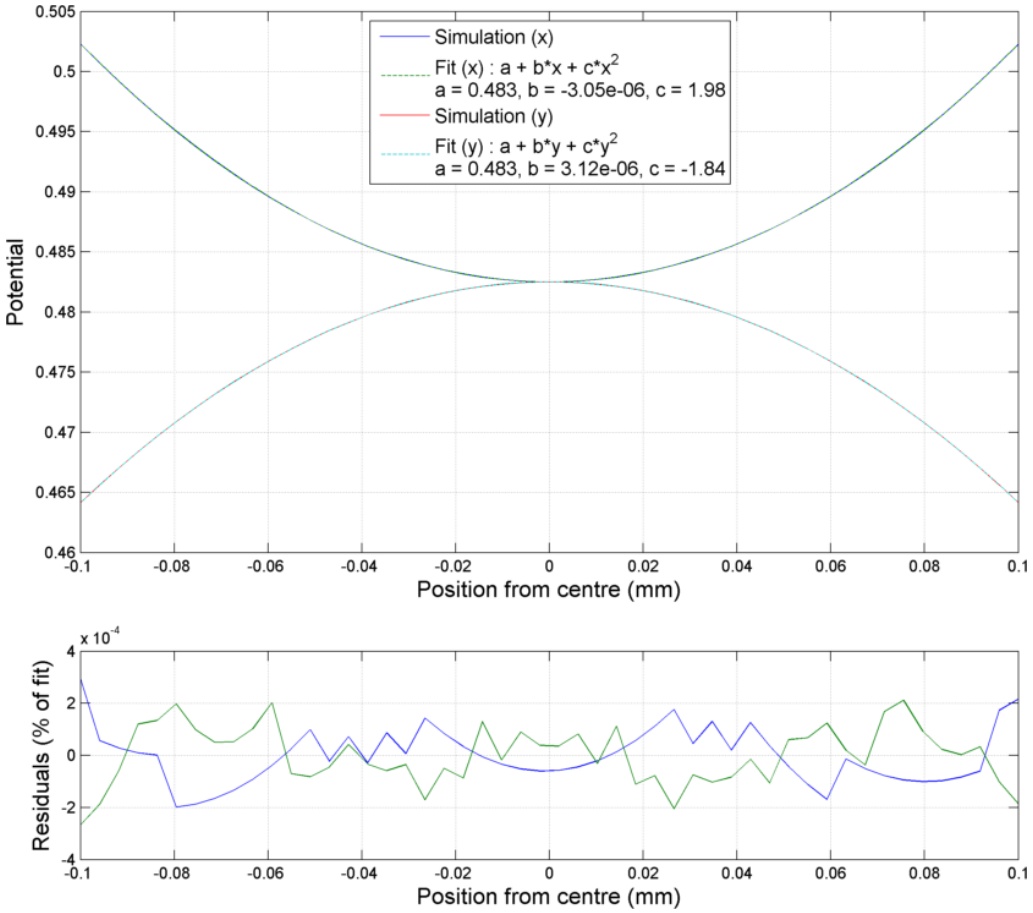

Figure 3.2: Simulated radial trap potential along $\hat{\mathbf{x}}$ ($y = z = 0$) and $\hat{\mathbf{y}}$ ($x = z = 0$), in the existing mark 2 linear trap geometry. $1\,\mathrm{V}$ is applied to one pair of blade electrodes, and all other electrodes are grounded.

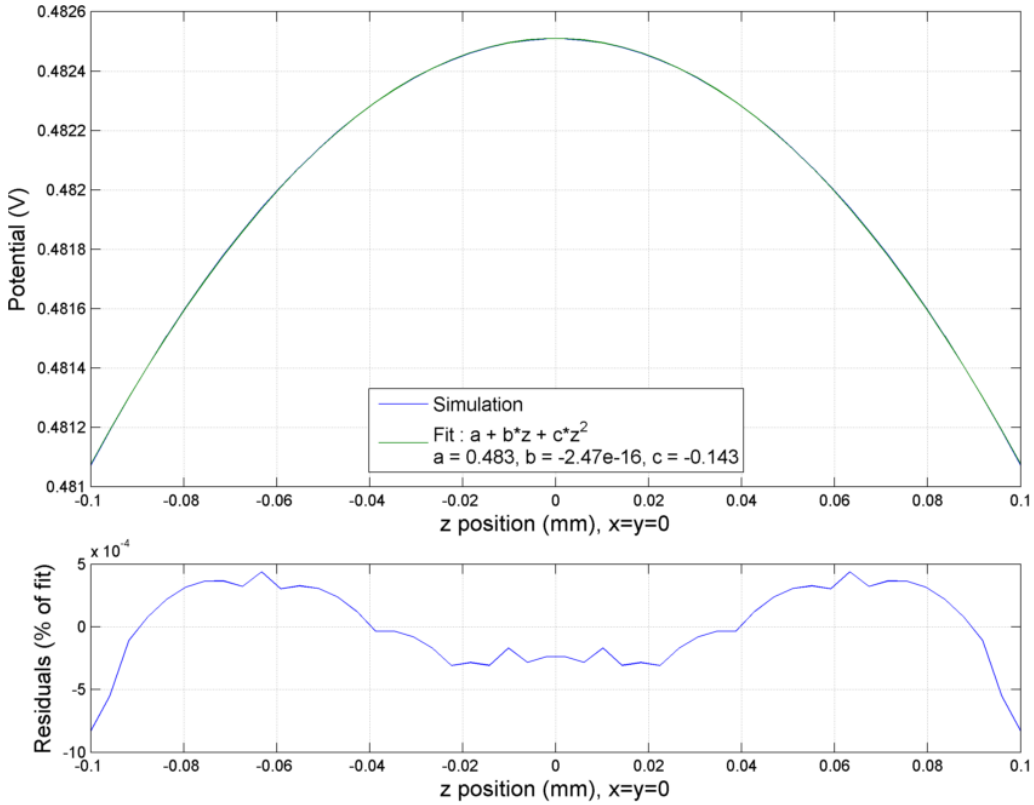

Figure 3.3: Simulated RF potential along the trap axis, $\hat{\mathbf{z}}$ ($x = y = 0$), in the existing mark 2 linear trap geometry. $1\,\mathrm{V}$ is applied to one pair of blade electrodes, and all other electrodes are grounded. It is this potential that leads to the axial micromotion discussed in section 2.2.

3.2 Simulation of new trap design

As noted in section 1.1, we expect the mark 3 linear trap geometry to be very similar to the existing mark 2 linear trap. From preliminary investigations we find that the dimension z_0 has the greatest influence on the axial micromotion. Hence we have chosen to change only this dimension, keeping all other trap geometry parameters constant.

In the following simulations we have ensured that the trap parameters are consistent with a stable linear ion crystal; see sections 2.3 and 2.4 for a full discussion.

3.2.1 Excitation spectrum

We examine two limiting cases: a two-ion crystal with $\omega_z = 2\pi \cdot 2\,\mathrm{MHz}, \omega_r = 2\pi \cdot 4\,\mathrm{MHz}$ (as discussed in section 2.4), where our main concern is individual ion addressing (see section 1.1.1) and so we wish to maximise the amplitude of the first micromotion sideband i.e. maximise $J_1(\beta)$, ideally $J_1(\beta) \gtrsim 0.1$; and an N-ion crystal with $\omega_z = 2\pi \cdot 1\,\mathrm{MHz}, \omega_r = 2\pi \cdot 5\,\mathrm{MHz}$, where our main aim is to perform the same operation on all ions in the crystal with high fidelity and so we wish to minimise the deviation in the carrier amplitude i.e. maximise $J_0(\beta)$ for the outermost ion in the crystal. Note that since $\beta = \sqrt{2}k_{397}d_z$, with $d_z = \dfrac{q_z\bar{z}}{2}$, and $J_0(\beta) \simeq 1 - \beta^2$ for $\beta \ll 1$, the outermost ion (with largest $\bar{z}$) will have the smallest carrier amplitude. Hence for large crystals we are concerned with the ratio of carrier amplitude between the outermost and innermost ion $J_0(\beta_{\text{outer}})/J_0(\beta_{\text{inner}})$. In practice, the innermost ion has a very low micromotion amplitude compared to the outermost, and so there is little difference between $J_0(\beta_{\text{outer}})$ and $J_0(\beta_{\text{outer}})/J_0(\beta_{\text{inner}})$. In figures 3.4 and 3.5 we have plotted $J_0(\beta_{\text{outer}})$ for simplicity.

As can be seen from figures 3.4 and 3.5, a compromise must be made between maximising $J_1(\beta)$ for the two-ion crystal and minimising $J_0(\beta)$ for the

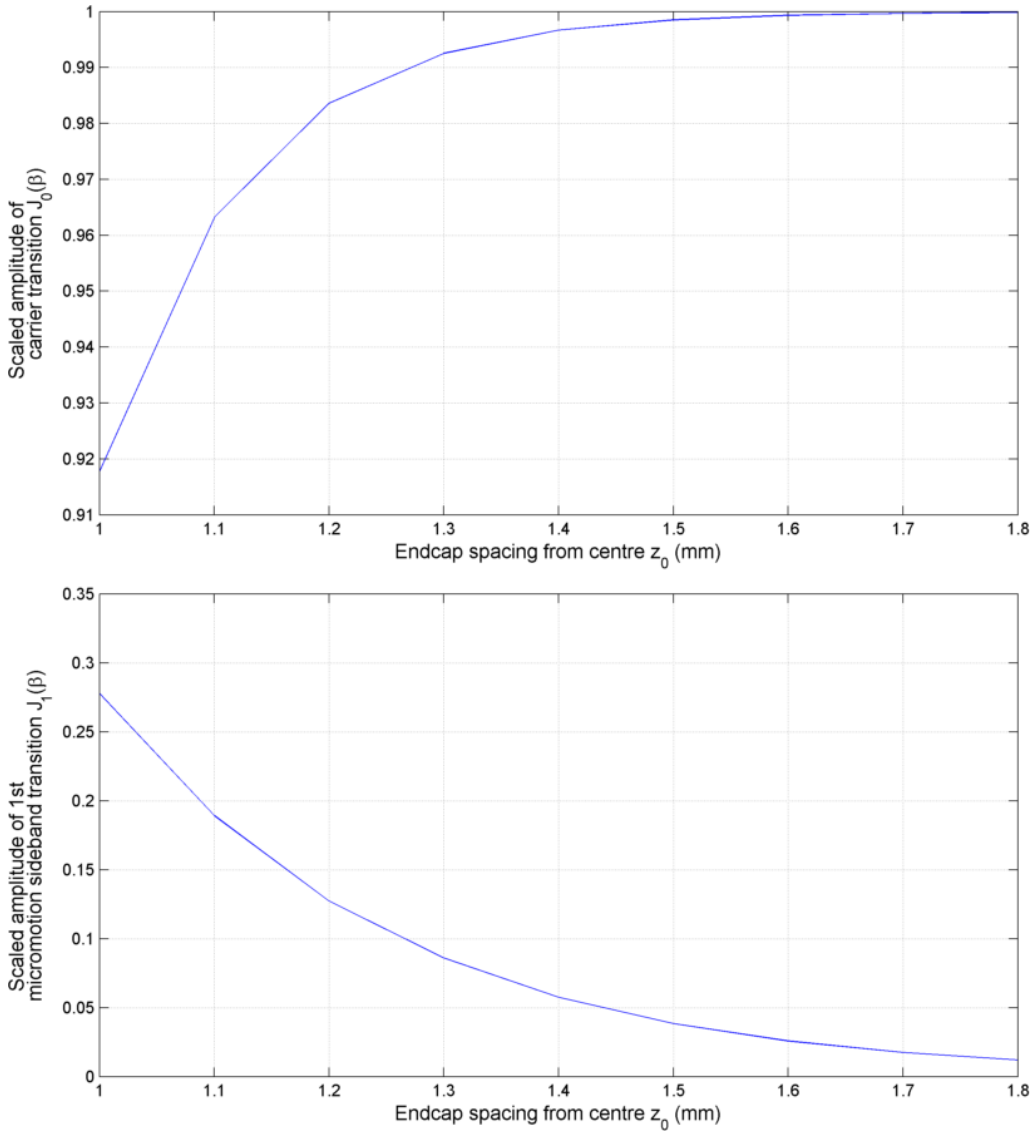

Figure 3.4: Scaled amplitude of carrier and first micromotion sideband in the ion excitation spectrum, as discussed in section 2.2.4, for the outermost ion in a 2-ion crystal with $\omega_z = 2\pi \cdot 2\,\mathrm{MHz}, \omega_r = 2\pi \cdot 4\,\mathrm{MHz}$. This gives $q_r = 0.40$ and $\alpha = 0.25$; see section 2 for definitions).

outermost ion in an N-ion crystal. This is due to the physical nature of the excitation spectrum; if the probability of excitation on the sidebands is increased, the probability of excitation on the carrier must be decreased so that the sum of probabilities is always unity. We therefore cannot fully achieve both objectives with the same trap geometry.

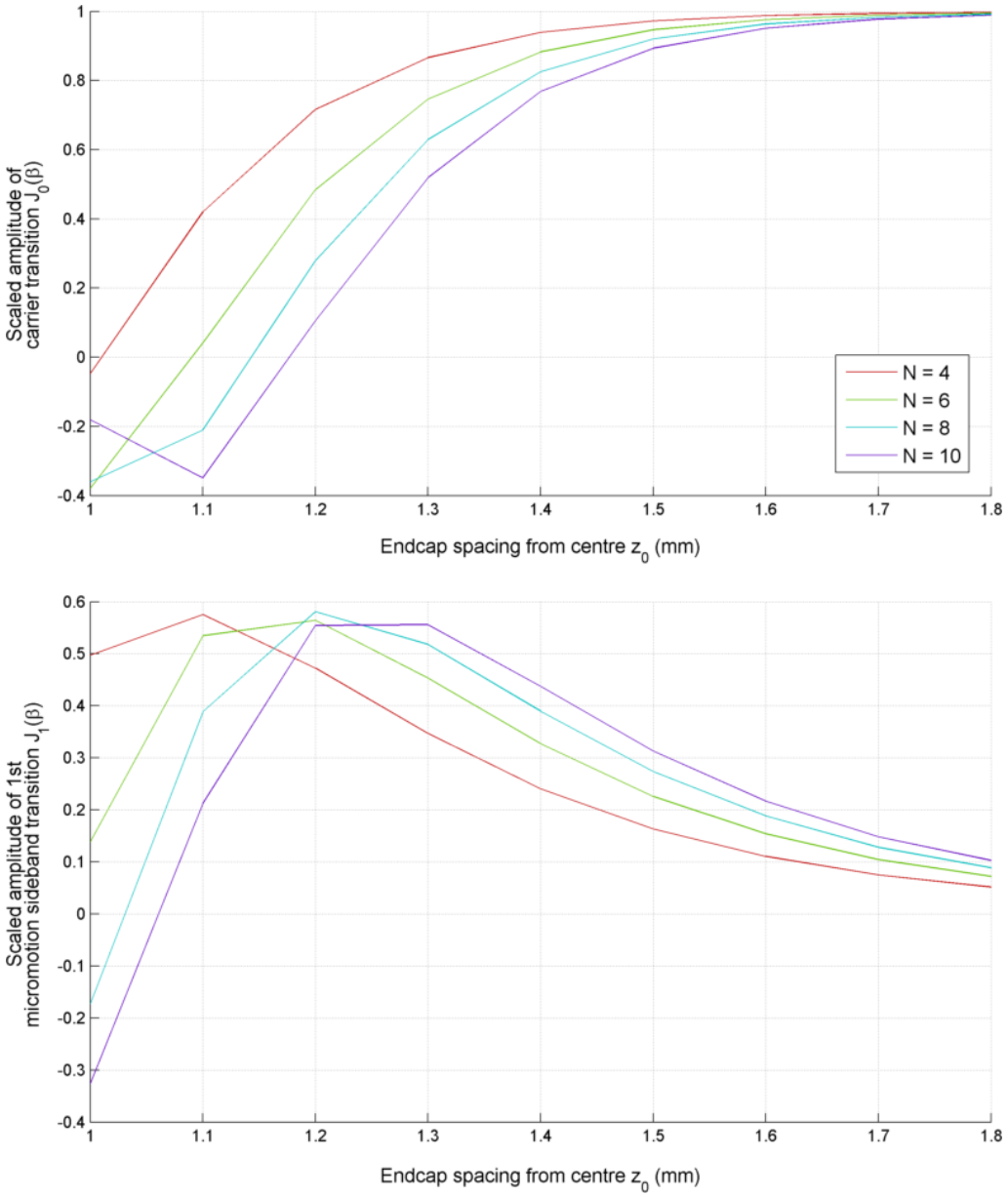

Figure 3.5: Scaled amplitude of carrier and first micromotion sideband in the ion excitation spectrum, for the outermost ion in an N-ion crystal with $\omega_z = 2\pi \cdot 1\,\mathrm{MHz}, \omega_r = 2\pi \cdot 5\,\mathrm{MHz}$. This gives $q_r = 0.48$ and $\alpha = 0.04$; see section 2 for definitions).

3.2.2 Electrode voltages

The trap supply voltages must be high-quality, accurate and stable to avoid electrical noise, which can cause anomalous heating, and drifts in the trap secular frequencies, which lower the fidelity of gate operations. This power must be

supplied to the trap electrodes through electrical feedthroughs into the vacuum system, which must also be high-quality, low loss and low noise, as well as small enough to fit into the mechanical design. This places limitations on the maximum acceptable voltages which can be supplied to the trap. We aim to keep $V_{dc}, V_{ac} \leq 1\,\mathrm{kV}$. Based on figure 3.6, this is achievable so long as $z_0 \lesssim 1.5\,\mathrm{mm}$. Note that V_{ac} is independent of z_0.

3.2.3 Additional addressing RF

We consider the possibility of using an additional RF field applied to the endcap electrodes to provide an alternative means of addressing the ions. This would allow the trap design to be optimised for an N-ion crystal, with minimal micromotion amplitude, without losing the ability to address the ions on micromotion sidebands. An RF potential with peak amplitude V_{address} and frequency Ω_{address} would be applied to the endcap electrodes as shown in figure 3.7, in addition to the trapping voltages described in section 2.1.

By analogy to the analysis in section 2.2, this generates a potential

$$V_{\text{address}} = Q_{\text{address}} \left[z^2 - \left(\frac{x^2 + y^2}{2} \right) \right] \cos(\Omega_{\text{address}} t) \tag{3.1}$$

where

$$Q_{\text{address}} = \frac{\alpha_z^{dc} V_{\text{address}}}{z_0^2} \tag{3.2}$$

resulting in axial micromotion with amplitude d_{address}, where

$$d_{\text{address}} = \frac{q_{\text{address}} \bar{z}}{2} \qquad\qquad q_{\text{address}} = \frac{4ZeQ_{\text{address}}}{m\Omega_{\text{address}}^2} \tag{3.3}$$

The laser field at frequency ω_l will undergo additional modulation due to this addressing axial micromotion, resulting in a carrier at ω_l and two sets of

sidebands: one at $\omega_l \pm n\Omega$ with amplitudes $E_n = E_{0z}J_n(\beta)$; and one at at $\omega_l \pm n\Omega_{\text{address}}$ with amplitudes $E_n = E_{0z}J_n(\beta_{\text{address}})$, where $\beta_{\text{address}} = \sqrt{2}k_{397}d_{\text{address}}$.

We simulated the effects of applying this additional RF field, using $V_{\text{address}} = 200\,\text{V}$ and $\Omega_{\text{address}} = 2\pi \cdot 13\,\text{MHz}$; the results are shown in figure 3.8, comparing the amplitude of the carrier and first micromotion sidebands for the trapping RF field and the additional addressing field. With these parameters, there is only a factor of 2 increase in the sideband amplitude for the addressing field over the trap RF field.

There are several issues associated with introducing an additional RF field to the trap; we will list some of them here. Great care must be taken to avoid resonances with any of the motional frequencies (all motional modes in the radial and axial directions, as well as sum and difference frequencies between them). The endcap electrode voltage is currently filtered to eliminate high-frequency noise, and so this filter would need to be modified to allow conduction of the addressing field at Ω_{address}. From a technical perspective, the additional RF source must be high-quality and low noise to avoid introducing any electrical noise which could impact the heating rate. It must also be stable to avoid errors resulting from drifts in Q_{address}. For an RF source at $200\,\text{V}$, this is a significant technical challenge. It can certainly be achieved, and indeed we must have such a high-quality source for the trap RF, but it may be too costly in time and money compared to the advantages gained. The setup of the current trap is also well established and known to work well. The full effects of adding an extra RF field are unknown; it could introduce experimental difficulties which hinder our ability to carry out high-fidelity experiments. This could outweigh any benefit gained by using the additional RF field for addressing.

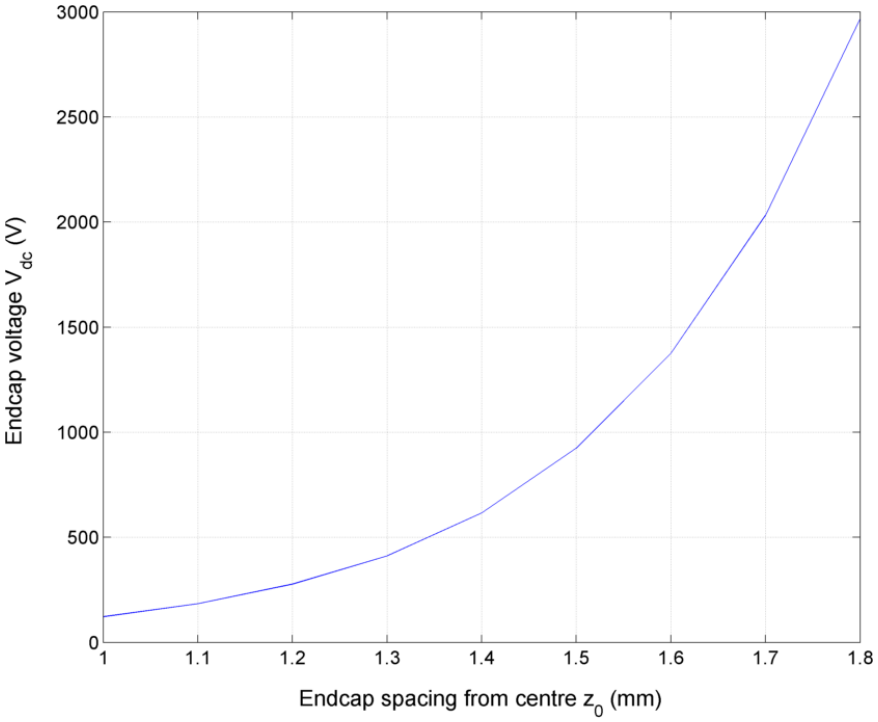

(a) DC endcap voltage V_{dc} required for $\omega_z = 2\pi \cdot 2\,\mathrm{MHz}$, $\omega_r = 2\pi \cdot 4\,\mathrm{MHz}$ (where $q_r = 0.40, \alpha = 0.25$). We find $V_{ac} = 780\,\mathrm{V}$, independent of z_0.

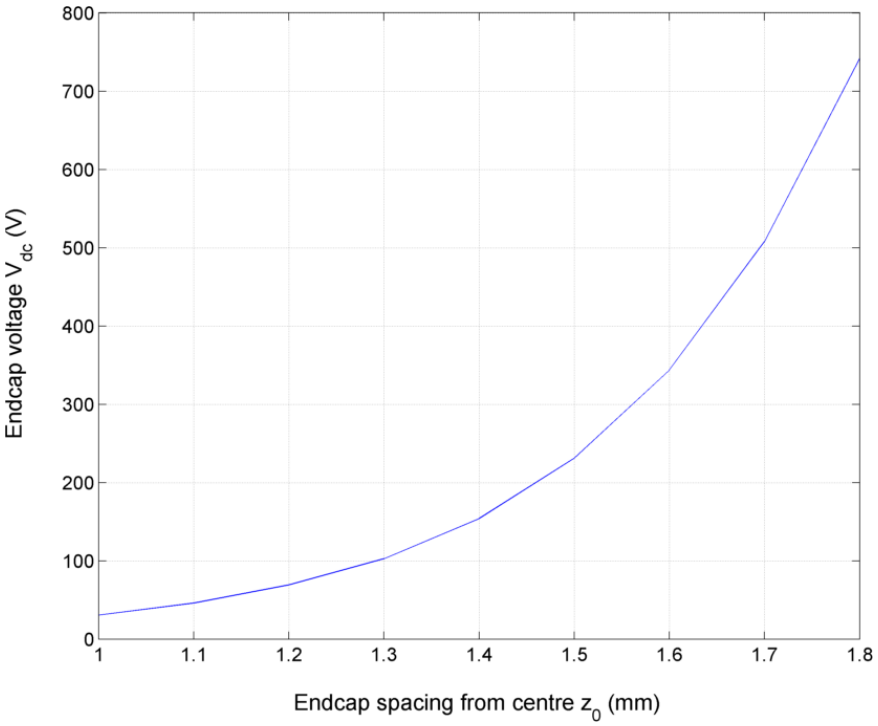

(b) DC endcap voltage V_{dc} required for $\omega_z = 2\pi \cdot 1\,\mathrm{MHz}$, $\omega_r = 2\pi \cdot 5\,\mathrm{MHz}$ (where $q_r = 0.48, \alpha = 0.04$). We find $V_{ac} = 980\,\mathrm{V}$, independent of z_0.

Figure 3.6: Simulated trap voltages

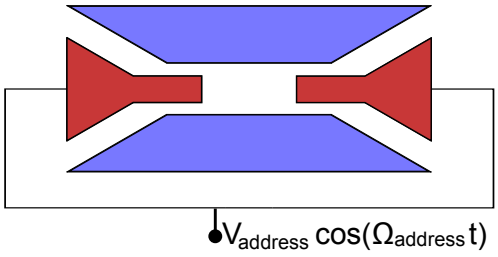

Figure 3.7: Additional RF potential applied to the endcap electrodes, proposed as an alternative means of addressing the ions using micromotion sidebands

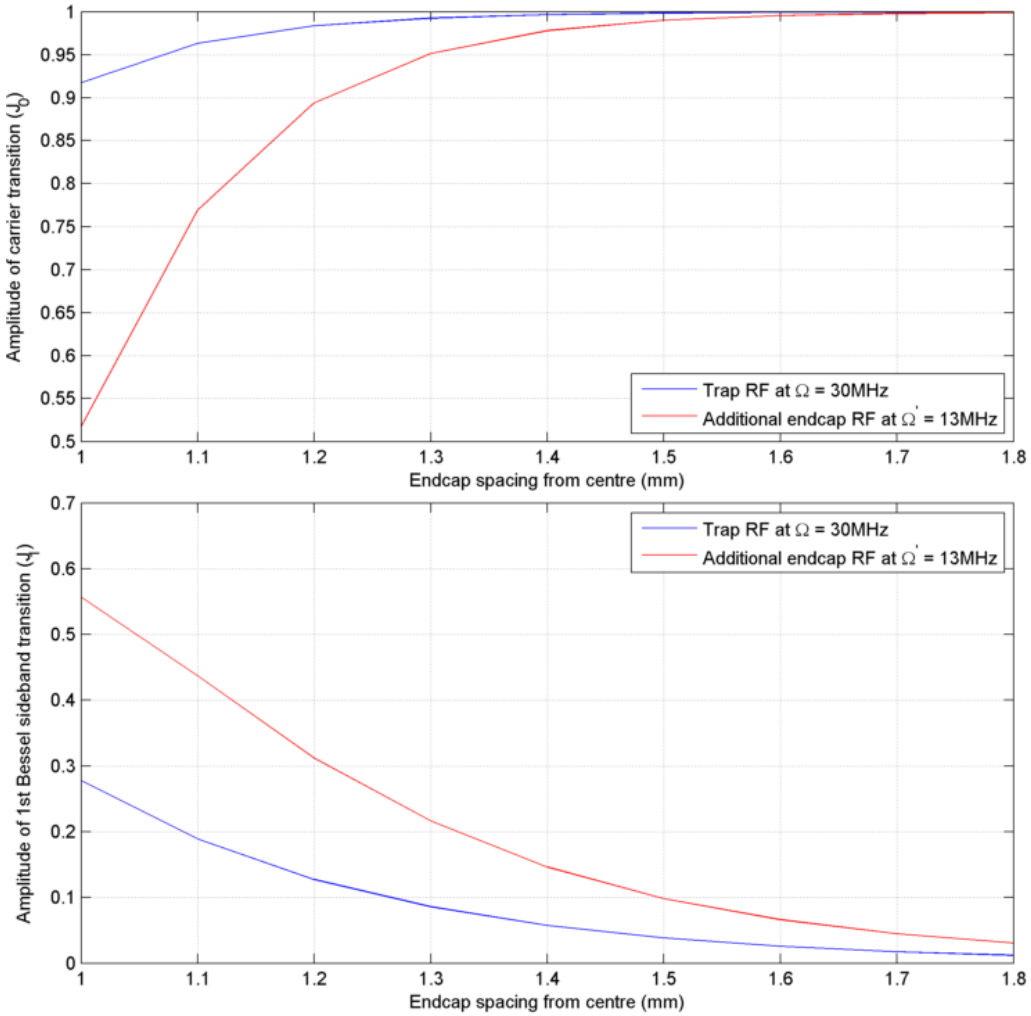

Figure 3.8: Amplitude of carrier and first micromotion sideband in the ion excitation spectrum for the outermost ion in a 2-ion crystal with $\omega_z = 2\pi \cdot 2\,\mathrm{MHz}, \omega_r = 2\pi \cdot 4\,\mathrm{MHz}$ ($q_r = 0.40$ and $\alpha = 0.25$), for (blue) the trap RF field, and (red) the extra addressing RF field.

4

Trap design

To achieve the changes outlined in section 1.1, a redesign of the trap was required. In particular, the NA $= 0.6$ objective lens requires an ion-window distance of $11\,\mathrm{mm}$. Since the mark 2 linear trap measures $16.6\,\mathrm{mm}$ from the trap axis to its highest point, the outside envelope of the trap must be reduced significantly in size to meet the new specifications.

4.1 Trap parameters

As discussed in section 1.1, we wish to maintain the desirable properties of our existing mark 2 linear trap. In particular, it has a low heating rate (1 quantum/s), which is important to avoid decoherence in the motional degree of freedom used to implement gates. Although many factors can contribute, we believe that the trap geometry (i.e. z_0, ρ_0, and the shape of electrodes close to the ion) is key in maintaining the existing heating rate. We therefore wish to keep the geometry of the electrodes roughly the same.

Based on the simulation and analysis in section 2, we have chosen an endcap spacing of $z_0 = 1.15\,\mathrm{mm}$. This is a compromise to prioritise addressing of individual ions using axial micromotion sidebands (see section 2.2.4), while keeping the carrier amplitudes as constant as possible across larger crystals. The design parameters for the mark 3 linear trap are shown in table 4.1.

z_0	$1.15\,\mathrm{mm}$
ρ_0	$0.5\,\mathrm{mm}$
α_x	0.486
α_y	0.487
α_z^{ac}	0.104
α_z^{dc}	0.207

Table 4.1: Design parameters for the mark 3 linear trap

4.2 Electrode alignment

To achieve an ion-window distance of $11\,\mathrm{mm}$, the overall size of the trap must be reduced. The existing mark 2 trap uses a combination of $1.6\,\mathrm{mm}$ diameter alignment pins and M1.6 bolts to attach the electrodes to the insulating Macor holders, and to align the electrodes relative to each other. With a smaller trap envelope, this arrangement will no longer be possible. In addition, the alignment on the mark 2 trap was mostly carried out by eye, with the pins and bolts holding the electrodes in place once aligned rather than guiding the process.

We determined that the alignment of the blade tips in the x-y plane (see figure 2.1 for axis definitions) was the most crucial consideration. Opposing blades should be exactly in line to minimise distortion of the RF trapping field. We decided to use a slot system to align the electrodes, as flat surfaces can be machined with higher tolerances than holes. When drilling holes it is very difficult to accurately specify the position, and there is some inaccuracy in the hole angle. In contrast, the slots to hold opposing blades can be machined with the same finishing cut, ensuring that they are parallel and well aligned.

The greatest restriction on manufacturing accuracy will be the machining of the Macor holders. The material is highly abrasive and wears the cutter material quickly, introducing errors. This can be somewhat mitigated by the use of several cutters, with a new cutter for the finishing cut. The Macor is also brittle and prone to cracking during machining, so care must be taken to avoid excess stresses on the material. We estimate manufacturing tolerances of $\sim 30\,\mu\mathrm{m}$ for

the Macor holders ($50\,\mu\mathrm{m}$ maximum), and 5-$10\,\mu\mathrm{m}$ for the steel electrodes. We therefore chose to manufacture the Macor pieces first, so that we can measure the resulting slot widths and specify the electrode dimensions to fit. For the mounting slot arrangement the absolute dimensions are fairly unimportant (to within $0.5\,\mathrm{mm}$), but the relative dimensions of the electrodes and holders are critical for a good fit.

4.3 Compensation electrodes

Due to manufacturing imperfections, we find that the centre of the trapping potential does not correspond to the geometric trap centre, and the axes of the DC and RF fields are not the same. To eliminate radial micromotion these must be well aligned, and so we introduce compensation electrodes, parallel to the trap axis, to allow a DC offset field to be added. This allows us to align the trapping potentials from the endcaps (DC) and blades (RF), as well as providing a method of radially translating the trapped ions. Note that axial translation can be achieved by adding offset potentials directly to the endcap voltages. The compensation electrodes in the mark 2 linear trap were positioned by hand, and we do not accurately know their positions. In the mark 3 linear trap we wish to specify the positions of the compensation electrodes so that we can accurately predict the resulting field.

The positioning of the compensation electrodes is limited by several factors. There must be adequate spacing to other electrodes to avoid breakdown across the vacuum or Macor. The dielectric strength of Macor is specified as $129\,\mathrm{kV\,mm^{-1}}$ for DC, and $45\,\mathrm{kV\,mm^{-1}}$ for AC [6], although this can be reduced by surface imperfections or dirt. Electrical breakdown across UHV gaps is typically limited by electrode shape (e.g. sharp edges) and surface imperfections or dirt, rather than distance. However, there must be sufficient distance between electrodes to allow for manufacturing imperfections and material deformation

under bakeout. Given maximum voltages of $1\,\mathrm{kV}$ on any electrode (limited by electrical feedthrough specifications), we have chosen a gap of $2\,\mathrm{mm}$ across Macor, and $0.5\,\mathrm{mm}$ across UHV. This allows an error margin of $\mathcal{O}(10^1)$ for AC and $\mathcal{O}(10^2)$ for DC on the specified breakdown values, which should be sufficient to allow for manufacturing tolerances and surface imperfections or dirt.

We must also ensure that the electrodes do not obstruct any potential laser beam paths, or the imaging system. To maximise the collection efficiency of the NA = 0.6 objective lens discussed in section 1.1.3 we choose not to place any compensation electrodes above the trap, between the ions and imaging system. The compensation electrodes must, as in the existing trap, be close enough to the trap axis to avoid shielding by the blade electrodes. Simulations were carried out as described in section 3, with the addition of compensation electrodes into the model, to understand the relationship between electrode positioning and resulting electric field at the trap centre. The results are shown in figure 4.1. It should be noted that this simulation has been carried out with a wire diameter of $0.5\,\mathrm{mm}$, whereas the electrodes will be $0.38\,\mathrm{mm}$ in diameter, however this difference has negligible effect on the results.

To choose a position for the compensation electrodes we considered a possible misalignment of up to $50\,\mu\mathrm{m}$, based on the guaranteed manufacturing tolerances for the Macor. Given the results in figure 4.2, and the availability of space near the trap centre, we have chosen to position the compensation electrodes at a radius of $3\,\mathrm{mm}$ from the trap axis. There will be one electrode at each side of the trap, below the laser beam paths, and one below the trap (seen in figure 5.1).

The existing compensation electrodes were mounted in the holders well away from the endcap electrodes, then bent in close to the trap axis (between 2 and $5\,\mathrm{mm}$ from the trap centre) to avoid shielding of the compensation field by the blade electrodes (figure 4.2a). We considered using the same design, however there were concerns about the accuracy and stability of the electrode positions.

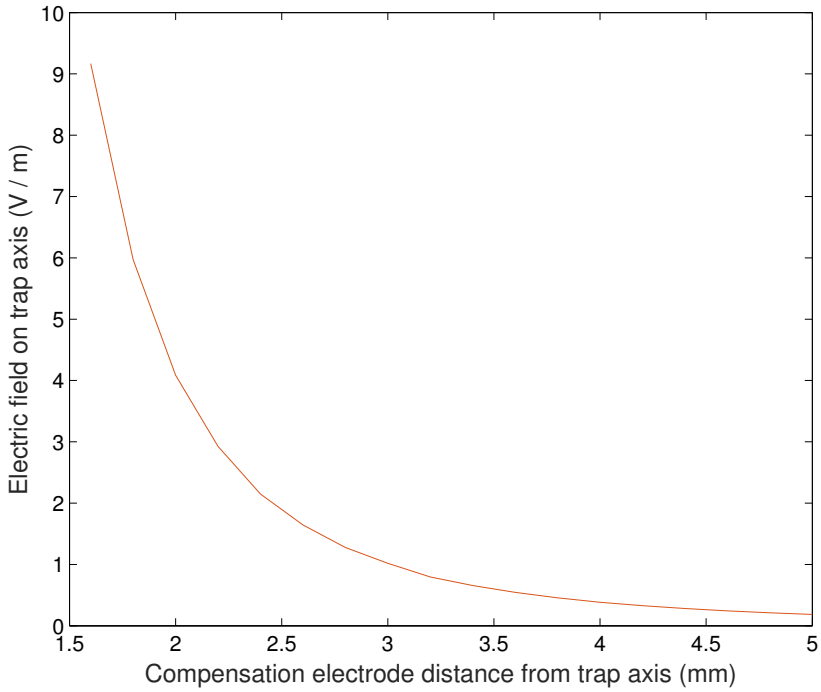

Figure 4.1: Electric field on trap axis from the straight compensation electrodes for the new trap, described in section 4.3. Note that the electrode distance measures to the centre of the wire.

It would be possible to bend the wire accurately using a template, but accurate mounting would be challenging as the wire can rotate in the mounting holes. This issue can be avoided by using straight wire electrodes, since they are rotationally symmetric. However, the mounting points must then be behind the 'skirt' at the base of the endcap electrodes, which shields the ion from any patch potentials which may build up on the insulating Macor surface. We decided to feed the compensation electrodes through a hole in the endcap skirt, since we estimate that this will result in an acceptably low risk of exposing the ions to patch potentials.

The electrodes will be made from straight $0.38\,\mathrm{mm}$ diameter tungsten wire. This diameter was chosen to minimise the size of the clearance holes in the endcap electrodes, while keeping the wire rigid enough to withstand trap assembly and baking without bending. $0.4\,\mathrm{mm}$ diameter stainless steel 316 (SS316) wire was initially chosen, however there were supply problems and so the $0.38\,\mathrm{mm}$

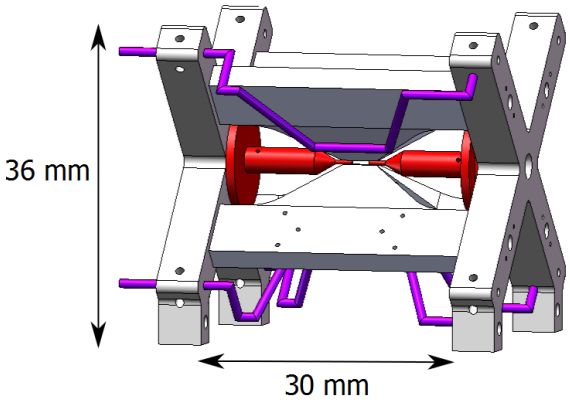

(a) Mark 2 linear trap design

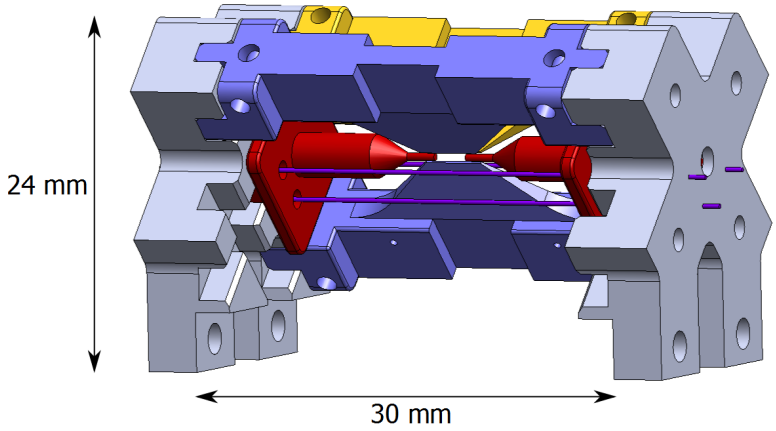

(b) Mark 3 linear trap design with one blade electrode hidden, showing the clearance holes in the endcap electrodes (in red)

Figure 4.2: CAD models for each of the mark 2 and 3 linear trap designs. Note the difference in scale. The compensation electrodes are shown in purple. In figure 4.2b the insulating Macor is shown in grey, and trap electrode colouring matches figure 2.1: endcap electrodes are shown in red, the blade electrodes in blue ($+V_{ac}\cos\Omega t$) and yellow (ground). In figure 4.2a the Macor is shown in white, the endcap electrodes in red and the blade electrodes in white.

diameter tungsten was suggested as an alternative. We believe it will actually be more suitable than the SS316 wire since the SS316 would be mechanically straightened from coiled stock, and therefore has no guaranteed level of straightness, whereas the tungsten is drawn as fully straight wire.

4.4 Microwave access

The existing mark 2 trap does not provide any dedicated access for transmitting microwaves. We currently apply $10\,\mathrm{W}$ of microwave power to a DC feedthrough connected to one end of a grounded blade electrode. This allows us to apply microwave pulses to the ions, but most of the power is reflected or dissipated before reaching the trap centre, which results in long pulse times and risks significant heating of the trap components. In the mark 3 trap we wish to include a more efficient method of delivering microwave power to the trapped ions. This will consist of a coaxial feedthrough specifically intended for use with microwave frequencies, which will connect to a microwave antenna.

The antenna will take the form of a small loop, with an area of approximately $100\,\mathrm{mm}^2$, oriented along the trap axis and in a position approximately symmetric with the lower compensation electrode. Although microwave fields behave differently from DC electric fields, it is expected that the level of shielding from the blade electrodes will be low enough to cause minimal difficulties. The antenna will be formed from $0.38\,\mathrm{mm}$ diameter tungsten wire, as for the compensation electrodes. The wire will be bent into place using a template to achieve a regular shape and spot welded directly onto the coaxial feedthrough, one end connected to the centre conductor and one to the shield.

5

Planned trap characterisation

Once the trap has been successfully built and set up to trap ions, we must be able to characterise the trap performance to assess how well the design criteria have been met. Here we briefly describe the methods we intend to use to characterise the most important features of the new design.

5.1 Axial micromotion

The axial ion micromotion amplitude can be measured by observing the Bessel sidebands described in section 2.2.4 using Raman spectroscopy. For a given axial trap strength (i.e. V_{dc}) we can measure the ion position using a CCD camera. We can then trap one ion, displaced by a known distance $\bar{z}$ along the trap axis. Measuring the excitation spectrum in frequency space, we expect to observe a carrier peak at ω_l and first micromotion sidebands at $\omega_l \pm \Omega$, where Ω is the RF frequency. Using the calculations in section 2.2, we can find the micromotion amplitude, $d_z = \frac{q_z \bar{z}}{2}$, from the observed amplitude of the first micromotion sidebands $E_1 = E_{0z} J_1(\beta)$, where E_{0z} is the amplitude of the carrier and $\beta = \sqrt{2} k_{397} d_z$. We can also observe how the sidebands change depending on axial trap strength (and therefore $\bar{z}$).

5.2 Magnetic field gradient

Before assembly, we can approximately characterise the level of electrode magnetisation. We have a blade electrode from the mark 2 linear trap which was machined as a spare, and should therefore have the same properties as the electrodes in the trap. Using a Hall probe, we have measured a maximum magnetic field of $0.8(1)\mathrm{G}$ near the surface. We have repeated the same measurement on the new blade electrodes, finding a maximum magnetic field of $0.02(5)\mathrm{G}$. We estimate that the Hall sensor used is sensitive to a minimum field of approximately $0.04\,\mathrm{G}$, so the measurement from the new blade electrodes would be consistent with zero magnetic field.

This suggests that the magnetic field gradient in the new trap will be substantially smaller than previously observed. Once we have trapped ions, we can calculate the field gradient from the difference in qubit frequency for two ions in a linear crystal along the trap axis. As in section 5.1, we can measure the ion axial separation for a given trap strength. With two ions located along the trap axis, we measure the probability of spin-flip of a single ion against laser detuning, as in figure 1.4, to find the difference in qubit frequency. The qubit frequency field-dependence is $2.45\,\mathrm{MHz\,G^{-1}}$ for the 'stretch' qubit $4\mathrm{S}_{1/2}^{\mathrm{F=4,M_F=+4}} \leftrightarrow 4\mathrm{S}_{1/2}^{\mathrm{F=3,M_F=+3}}$ in $^{43}\mathrm{Ca}^{+}$, which we currently use, and so we can find the magnetic field gradient.

5.3 Optical access

The numerical aperture of the imaging system is set by the optical components and the geometry. On assembling the trap we will verify that the distance from trap centre to window is the desired $11\,\mathrm{mm}$. As described in section 4.3, we expect some misalignment of the electrodes due to manufacturing imperfections, and as a result the centre of the trapping potential is unlikely to be aligned

perfectly with the geometric trap centre. However this effect is expected to be $\mathcal{O}(10\,\mu\mathrm{m})$, and so will not impact significantly on the imaging system performance. The limitations are likely to come from manufacturing tolerances of the vacuum system and window, resulting in an expected deviation of $\pm 0.1\,\mathrm{mm}$ on the specified $11\,\mathrm{mm}$ dimension. Another limiting factor may be the obstruction of the aperture by trap electrodes, since the NA = 0.6 objective lens has a wide opening angle of 73.3° (see figure 5.1). In order to minimise this the blade tip width has been reduced to $0.15\,\mathrm{mm}$, and the blade divergence angle to $8.25°$. It is difficult to completely avoid any obstruction by the blade electrodes, but we estimate that such an obstruction will reduce the collection efficiency by $< 0.5\%$.

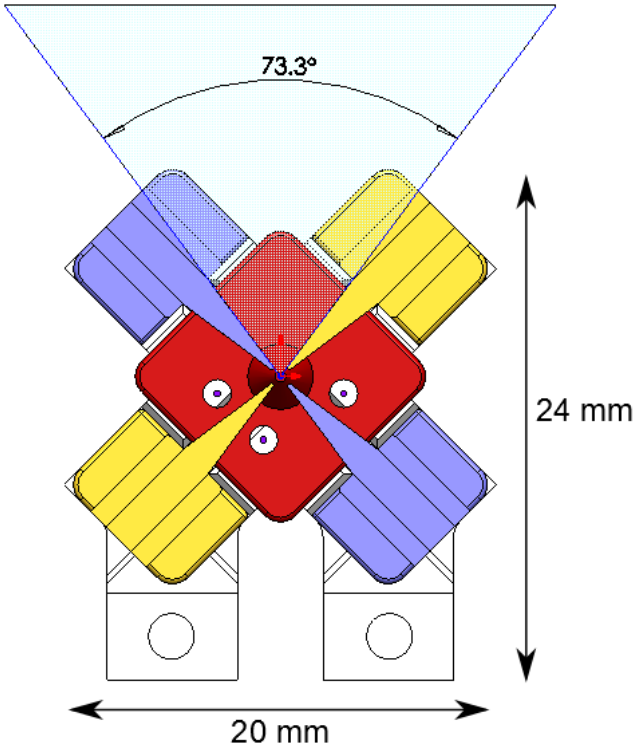

Figure 5.1: End-on view of the mark 3 linear trap, showing in light blue the opening angle for the proposed NA = 0.6 objective lens. The blade electrodes have been redesigned to minimise obstruction of this view. The insulating Macor is shown in white, and trap electrode colouring matches figure 2.1: endcap electrodes are shown in red, the blade electrodes in blue ($+V_{ac}\cos\Omega t$) and yellow (ground). The compensation electrodes (running parallel to the trap axis) are shown in purple.

6

Conclusions

We have identified some key areas for improvement in our existing linear blade Paul trap. Using a Mathieu equation approach, we have studied the theory behind axial ion micromotion, understanding how it is influenced by trap geometry and its effect on the ions' excitation spectra. Carrying out electrostatic simulations to characterise the micromotion in our trap geometry, we have shown that a compromise must be reached between a large micromotion amplitude, allowing sideband addressing, and a small amplitude, allowing high fidelity operations on linear crystals of up to 10 ions. For the next iteration of our trap, the mark 3 linear trap, we have chosen a relatively large micromotion amplitude to prioritise the sideband addressing, set primarily by the endcap position z_0 along the trap axis. We have considered the presence of a magnetic field gradient in the existing mark 2 trap, and the limitations this places on the preparation of an entangled Bell state. We have identified the material and machining techniques used for the electrodes as a potential source, and considered how we can minimise the magnetic field in the new mark 3 trap. Preliminary measurements indicate we have significantly reduced magnetisation of the electrodes.

We have redesigned the mechanical structure of the trap to allow for a high NA objective lens to be used, to maximise photon collection efficiency with a view to carrying out ion-photon entanglement experiments. The mechanical design has been carefully considered to minimise errors in manufacturing pre-

cision, with a new electrode mounting system to ensure the electrodes are well-aligned and also that the alignment is repeatable. This will be of great benefit for ease of assembly, and to ensure consistency in future traps. Provision for a dedicated microwave antenna has also been included in the design.

The trap fabrication and assembly is complete, and we have carefully considered how the trap will be characterised once it is under vacuum and installed in the lab. Figure 6.1 shows the trap assembled and mounted on the base of the vacuum system. A prototype was manufactured and assembled to test out the new mechanical design, leading to some design improvements. Based on the prototype we are optimistic that the new trap will successfully meet the design aims, allowing us to carry out yet higher fidelity quantum operations and to implement a remote entangling link between two traps.

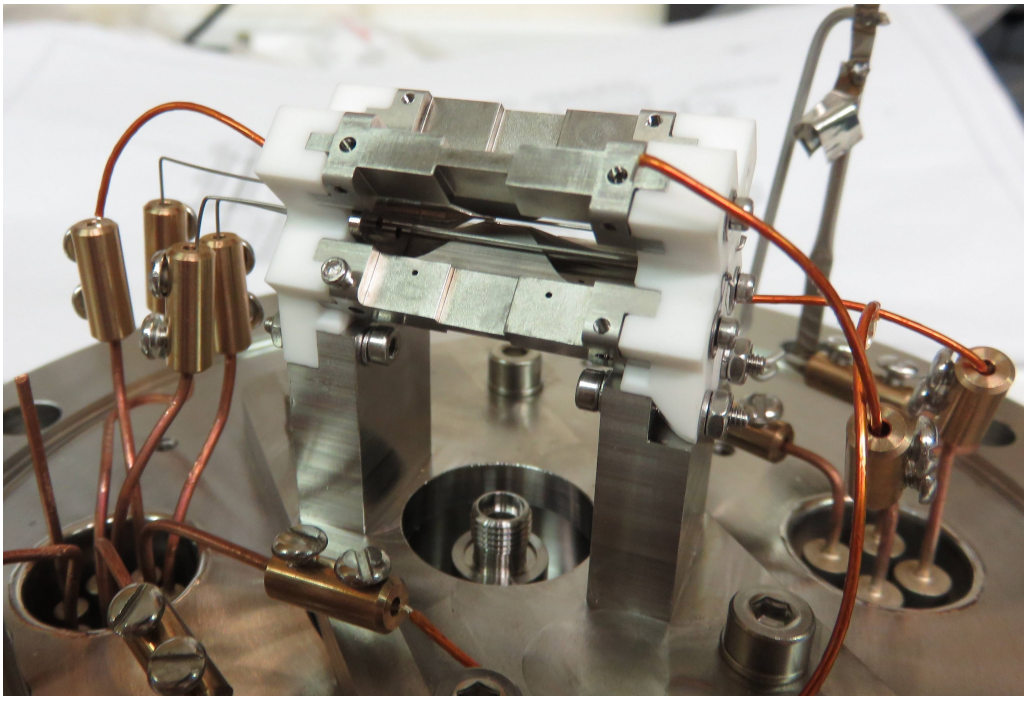

Figure 6.1: Photo of the finished trap, assembled and mounted on the base of the vacuum system. (Photo courtesy of K. Thirumalai)

Bibliography

[1] British Stainless Steel Association. Mechanism and measurement of work hardening of austenitic stainless steels during plastic deformation, May 2015.

[2] C. J. Ballance, T. P. Harty, N. M. Linke, and D. M. Lucas. High-fidelity two-qubit quantum logic gates using trapped calcium-43 ions. *ArXiv e-prints*, June 2014.

[3] C. J. Ballance, V. M. Schafer, J. P. Home, D. J. Szwer, S. C. Webster, D. T. C. Allcock, N. M. Linke, T. P. Harty, D. P. L. Aude Craik, D. N. Stacey, A. M. Steane, and D. M. Lucas. Hybrid quantum logic and a test of Bell's inequality using two different atomic species. *ArXiv e-prints*, May 2015.

[4] Christopher Ballance. High-fidelity quantum logic in Ca^+. D.Phil. Thesis, Oxford University, 2014.

[5] D. J. Berkeland, J. D. Miller, J. C. Bergquist, W. M. Itano, and D. J. Wineland. Minimization of ion micromotion in a paul trap. *Journal of Applied Physics*, 83(10), 1998.

[6] Corning. *MACOR*, 2012.

[7] D. Deutsch. Quantum Theory, the Church-Turing Principle and the Universal Quantum Computer. *Proc. R. Soc. Lond. A*, 400(1818):97–117, 1985.

[8] Charles Donald. Development of an ion trap quantum information processor. D.Phil. Thesis, Oxford University, 2000.

[9] D. Hucul, I. V. Inlek, G. Vittorini, C. Crocker, S. Debnath, S. M. Clark, and C. Monroe. Modular entanglement of atomic qubits using photons and phonons. *Nat Phys*, 11(1):37–42, Jan 2015. Letter.

[10] D.F.V. James. Quantum dynamics of cold trapped ions with application to quantum computation. *Applied Physics B: Lasers and Optics*, 190:181–190, 1998.

[11] C. Marquet, F. Schmidt-Kaler, and D.F.V. James. Phonon-phonon interactions due to non-linear effects in a linear ion trap. *Applied Physics B: Lasers and Optics*, 76(3):199–208, March 2003.

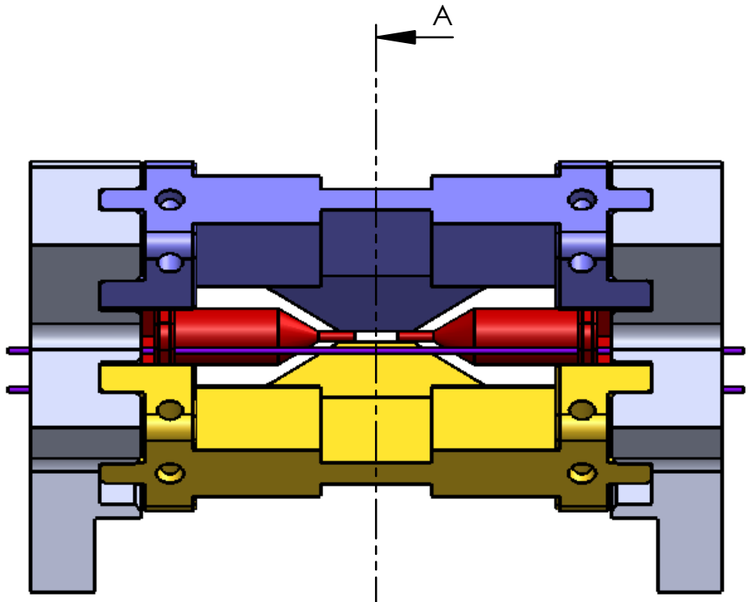

SECTION A-A

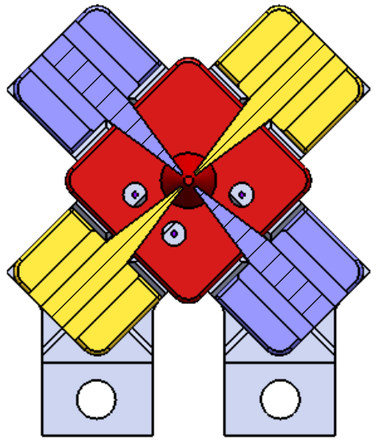

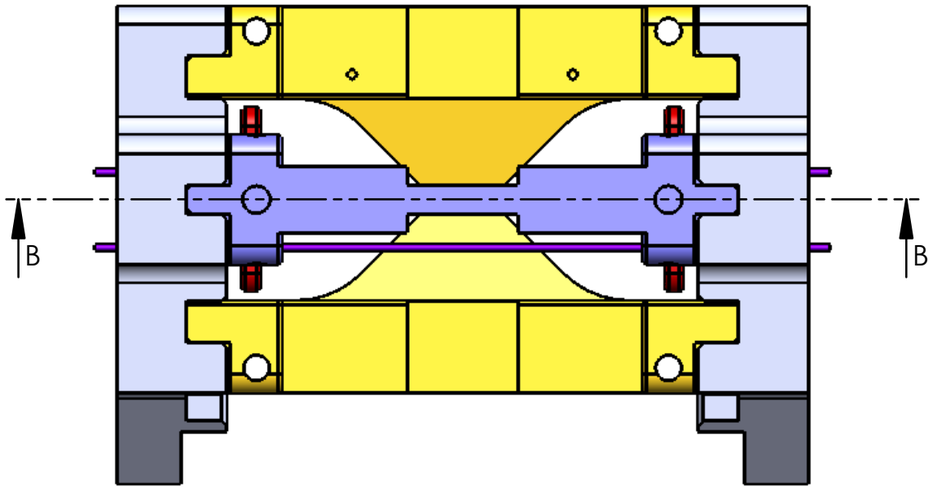

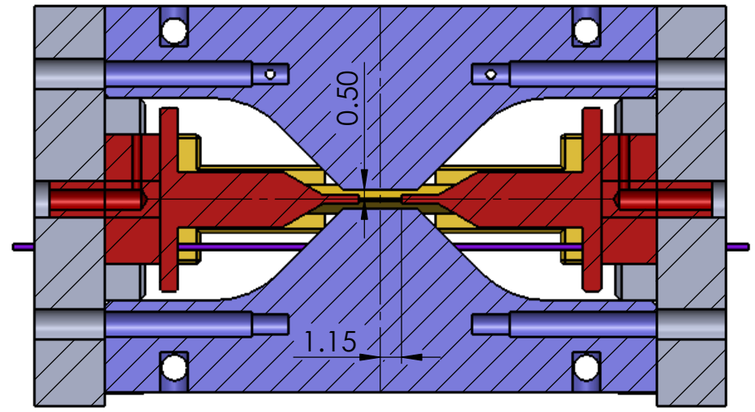

SECTION B-B

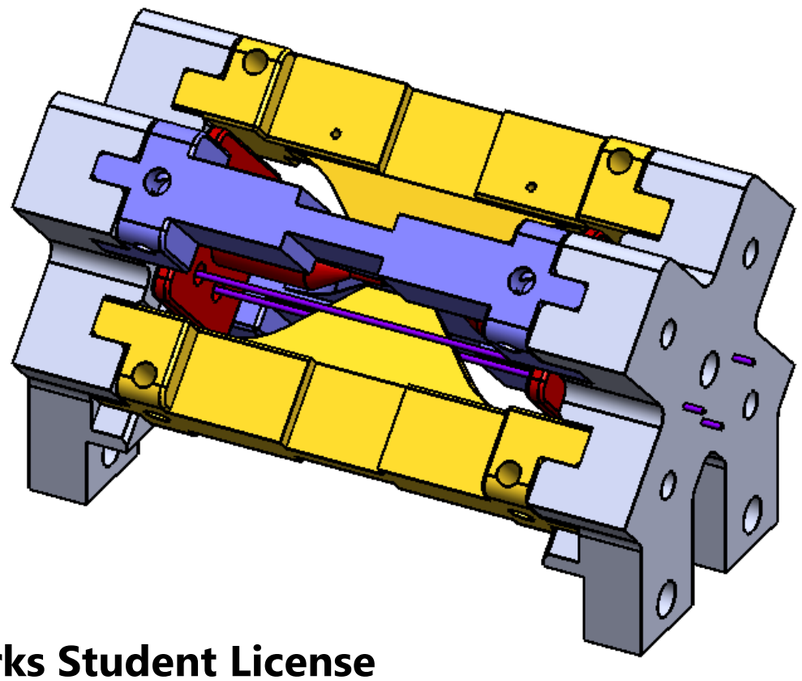

SolidWorks Student License
Academic Use Only

UNLESS OTHERWISE SPECIFIED: DIMENSIONS ARE IN MILLIMETERS SURFACE FINISH: TOLERANCES: LINEAR: ANGULAR:		FINISH:				DEBUR AND BREAK SHARP EDGES	DO NOT SCALE DRAWING / REVISION
	NAME	SIGNATURE	DATE				TITLE:
DRAWN							
CHK'D							
APPV'D							
MFG							
Q.A				MATERIAL:			DWG NO. Ion trap - assembled / A3
				WEIGHT:			SCALE:3:1 / SHEET 1 OF 1

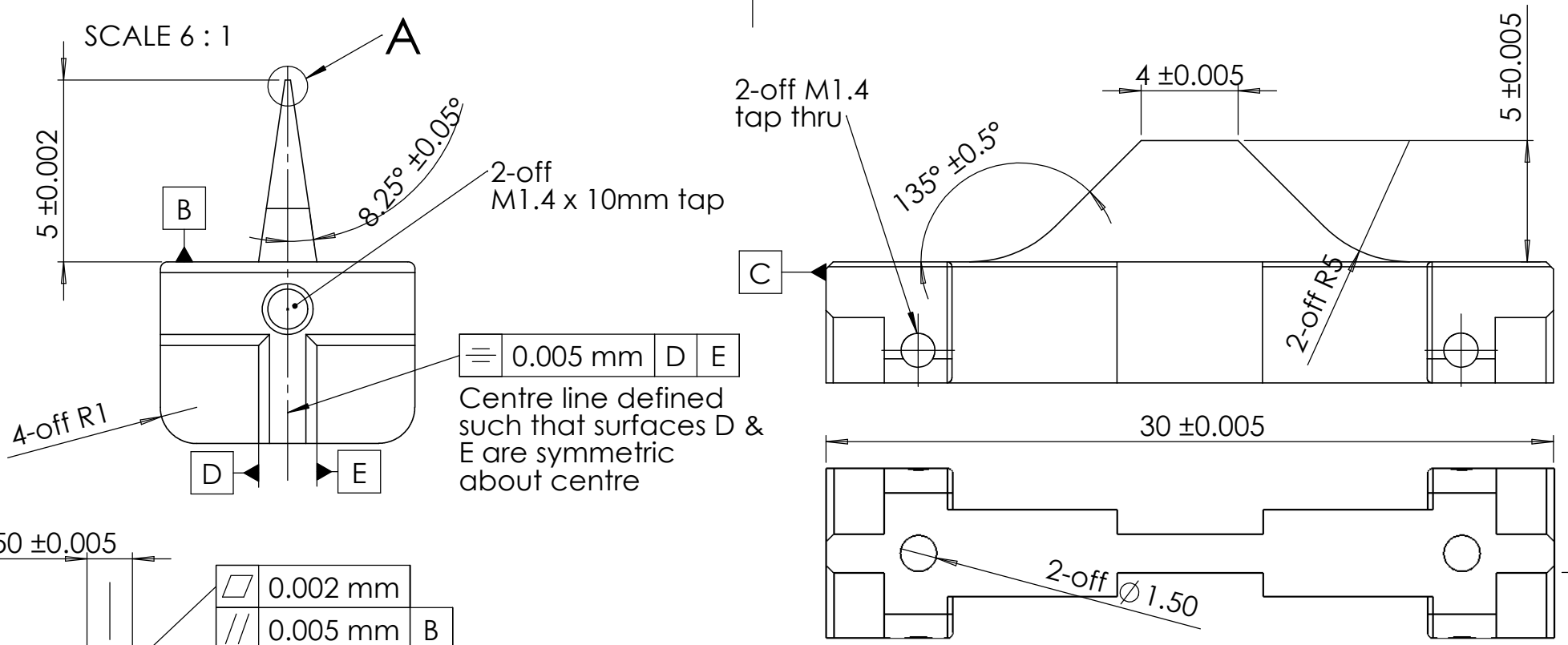

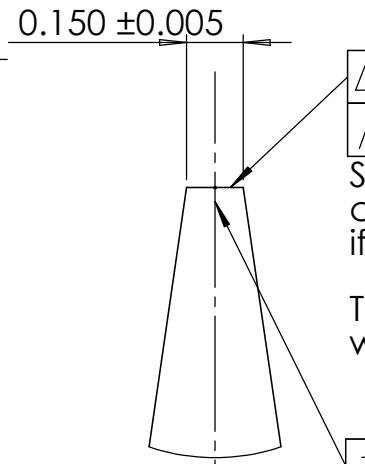

Surface finish on top face of blade tip is crucial - must be flat to within 2 microns if possible.

Top face of blade tip should be parallel to datums B and C to within 5 microns (see sheet 2 for datum specifications)

Blade tip must be symmetric about centre line

DETAIL A
SCALE 50 : 1

If anything is at all unclear, or any tolerances cannot be met, please contact Sarah before proceeding
sarah.woodrow@physics.ox.ac.uk
Ext 72265

UNLESS OTHERWISE SPECIFIED: DIMENSIONS ARE IN MILLIMETERS SURFACE FINISH: TOLERANCES: LINEAR: ANGULAR:		FINISH:			DEBUR AND BREAK SHARP EDGES	DO NOT SCALE DRAWING / REVISION
	NAME	SIGNATURE	DATE			TITLE:
DRAWN						
CHK'D						
APPV'D						
MFG						
Q.A				MATERIAL:		DWG NO. Ion trap - blade 1 / A4
				WEIGHT:		SCALE:4:1 / SHEET 1 OF 1

SCALE 6 : 1

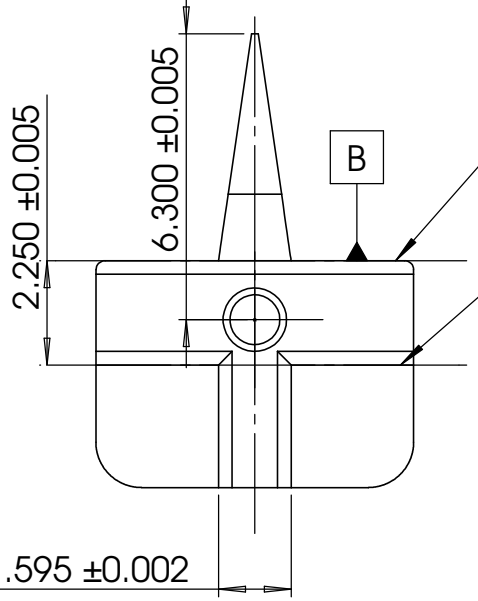

5-off 0.3mm chamfer at each end

//	0.005 mm
▱	0.005 mm

These surfaces must be flat and parallel to within 5 microns - marked by two horizontal centre lines - both ends

NB This dimension differs from the 3d model given

Surface properties of the end profile and surface B (flat, parallel, perpendicular) are crucial within 2.5mm from each end i.e. within these areas

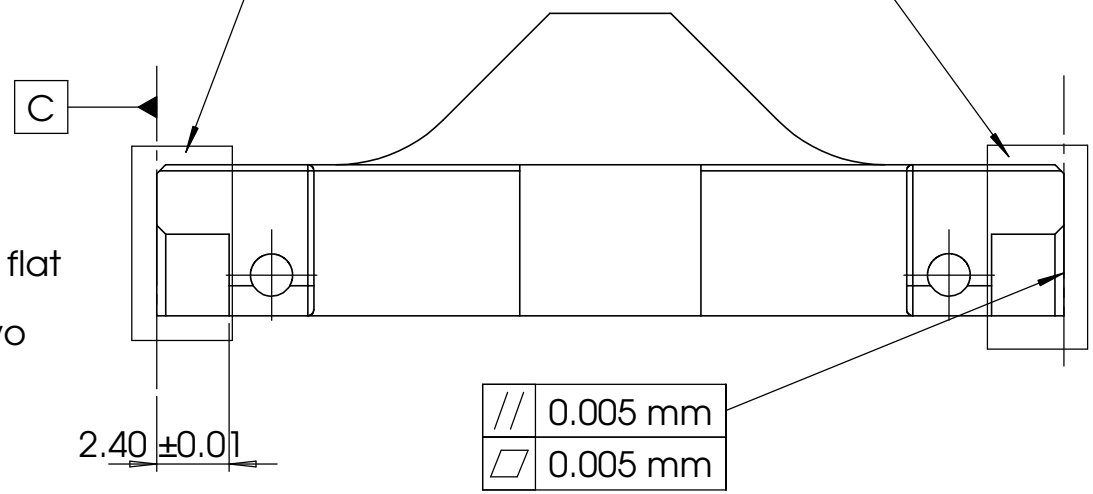

//	0.005 mm
▱	0.005 mm

End surfaces must be parallel and flat to within 5 microns - marked by 2 vertical centre lines

▱	0.005 mm
//	0.005 mm

These surfaces must be flat and parallel to within 5 microns - marked by 2 vertical centre lines - both ends

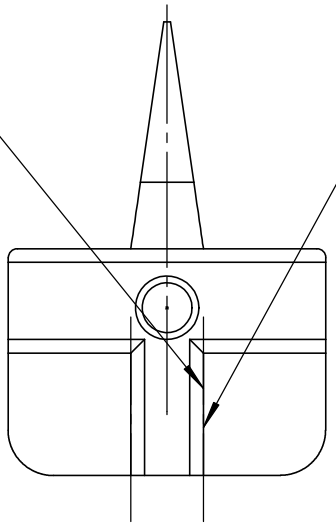

SCALE 6 : 1

⊥	0.005 mm	B C

Surfaces must be perpendicular to one another to within 5 microns - both ends

i.e. end profile shape must be square

If anything is at all unclear, or any tolerances cannot be met, please contact Sarah before proceeding
sarah.woodrow@physics.ox.ac.uk
Ext 72265

UNLESS OTHERWISE SPECIFIED: DIMENSIONS ARE IN MILLIMETERS SURFACE FINISH: TOLERANCES: LINEAR: ANGULAR:		FINISH:		DEBUR AND BREAK SHARP EDGES	DO NOT SCALE DRAWING	REVISION
	NAME	SIGNATURE	DATE			
DRAWN						
CHK'D						
APPV'D						
MFG						
Q.A				MATERIAL:	DWG NO. Ion trap - blade 2	A4
				WEIGHT:	SCALE:4:1	SHEET 1 OF 1

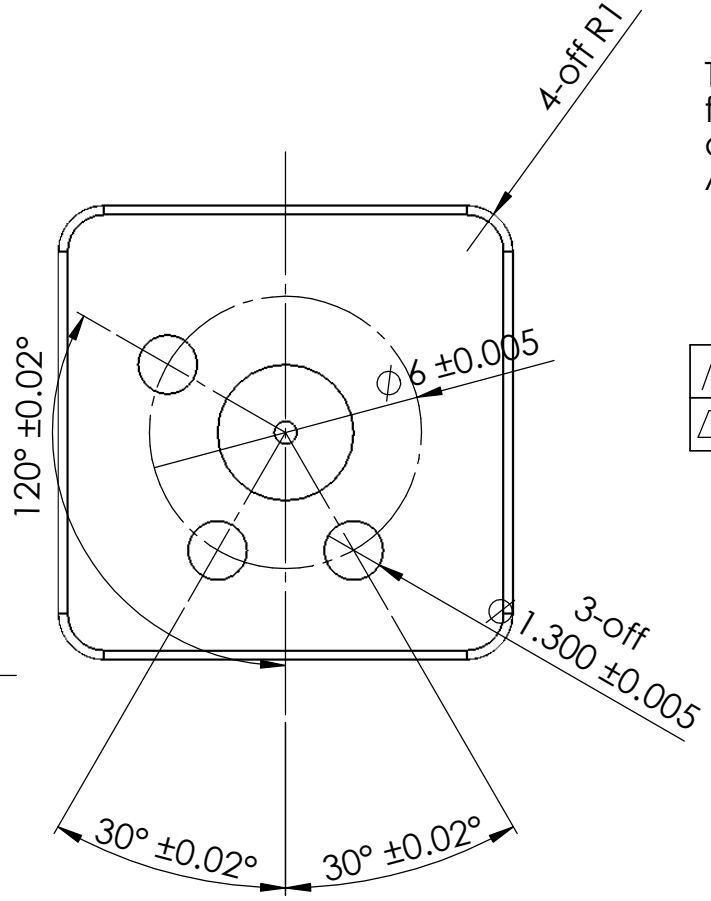

Tip surface must be flat to within 2 microns, and parallel to datum A to within 5 microns

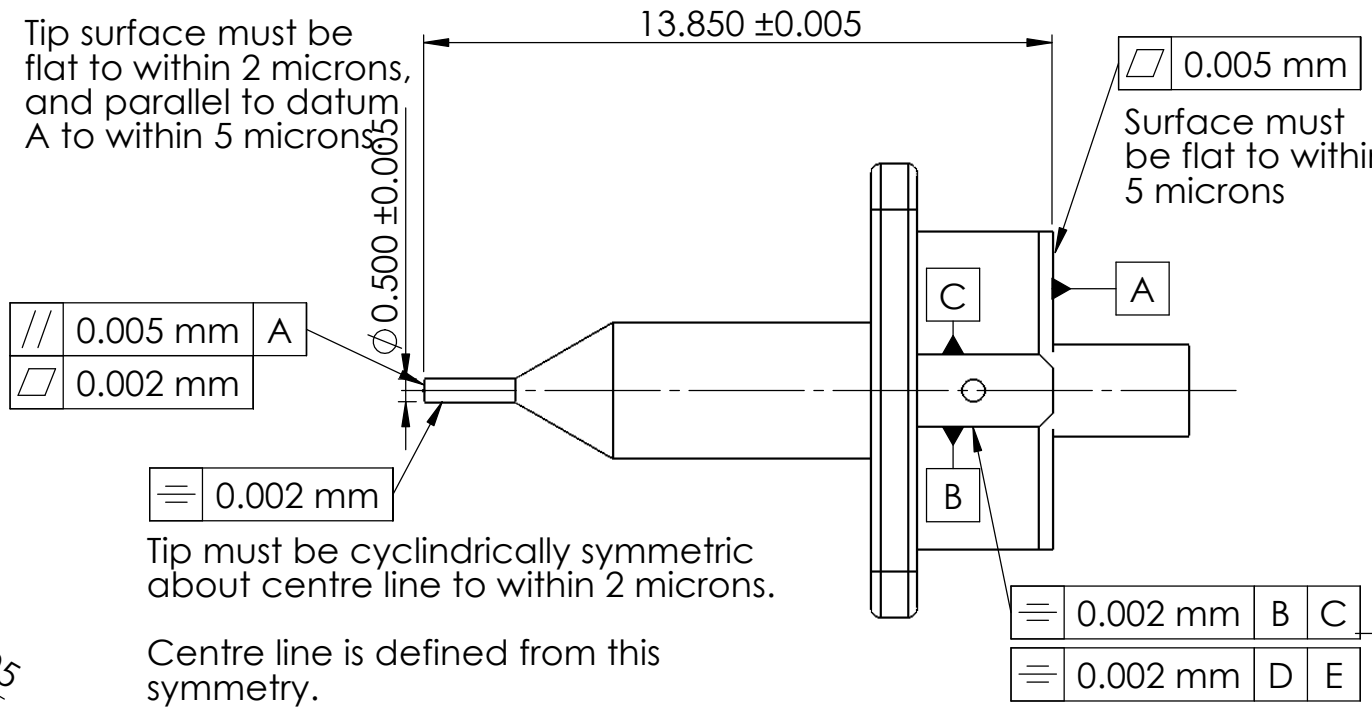

Tip must be cyclindrically symmetric about centre line to within 2 microns.

Centre line is defined from this symmetry.

Datums B and C must be symmetric about centre line to within 2 microns

Datums D and E must also be symmetric about centre line (see sheet 2 for datum definitions)

If anything is at all unclear, or any tolerances cannot be met, please contact Sarah before proceeding
sarah.woodrow@physics.ox.ac.uk
Ext 72265

UNLESS OTHERWISE SPECIFIED: DIMENSIONS ARE IN MILLIMETERS SURFACE FINISH: TOLERANCES: LINEAR: ANGULAR:		FINISH:			DEBUR AND BREAK SHARP EDGES	
	NAME	SIGNATURE	DATE			
DRAWN						
CHK'D						
APPV'D						
MFG						
Q.A				MATERIAL:		
				WEIGHT:		

DO NOT SCALE DRAWING | REVISION

TITLE:

DWG NO. Ion trap - endcap 1 A4

SCALE:6:1 | SHEET 1 OF 1

If anything is at all unclear, or any tolerances cannot be met, please contact Sarah before proceeding
sarah.woodrow@physics.ox.ac.uk
Ext 72265

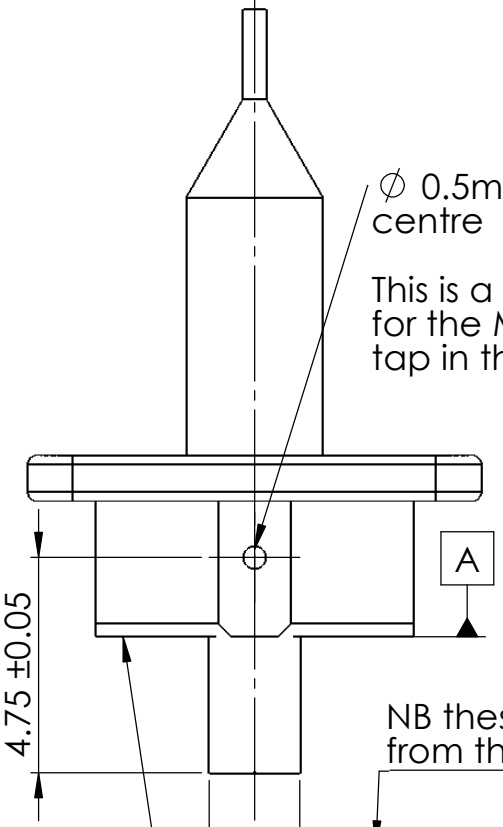

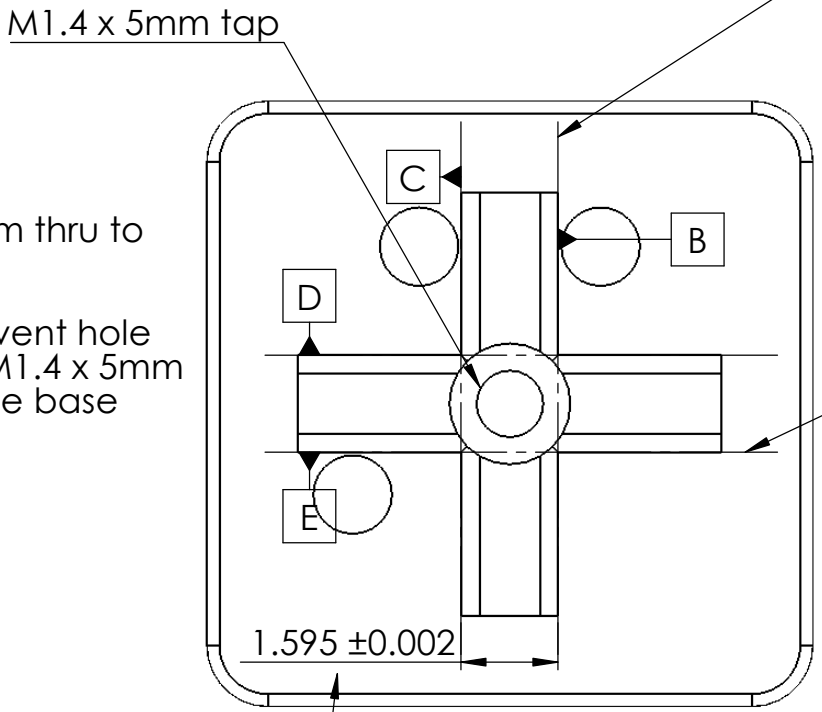

▱	0.005 mm	⌒	0.005 mm
//	0.005 mm		

Sides of the cross piece must be flat and parallel to within 5 microns - marked by 2 vertical centre lines.

The two opposing sides of the cross should be in line to within 5 microns

▱	0.005 mm	⌒	0.005 mm		
//	0.005 mm	⊥	0.005 mm	A	B

The conditions described above must also be met for the horizontal sides of the cross piece - marked by 2 horizontal centre lines.

These surfaces should also be perpendicular to surfaces A and B to within 5 microns

i.e. the profile shape of the cross piece, used for mounting, must be square

UNLESS OTHERWISE SPECIFIED: DIMENSIONS ARE IN MILLIMETERS SURFACE FINISH: TOLERANCES: LINEAR: ANGULAR:		FINISH:		DEBUR AND BREAK SHARP EDGES		DO NOT SCALE DRAWING	REVISION
	NAME	SIGNATURE	DATE			TITLE:	
DRAWN							
CHK'D							
APPV'D							
MFG							
Q.A				MATERIAL:		DWG NO. Ion trap - endcap 2	A4
				WEIGHT:		SCALE:8:1	SHEET 1 OF 1

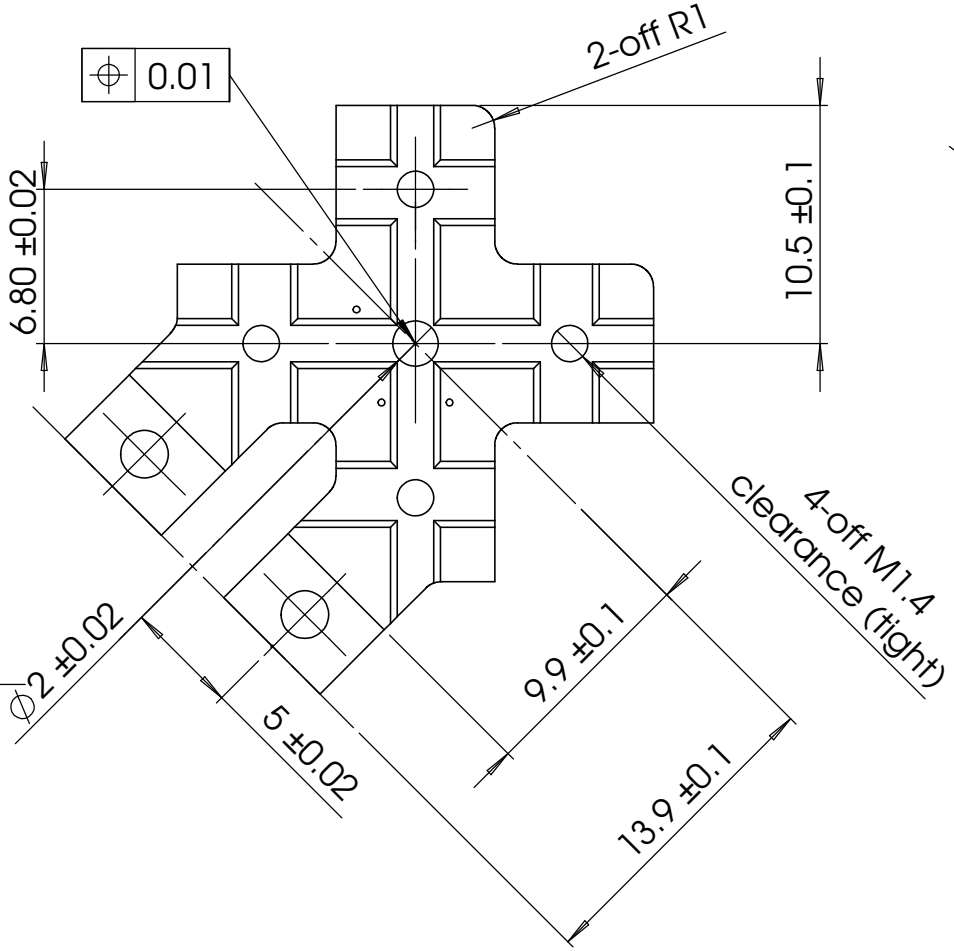

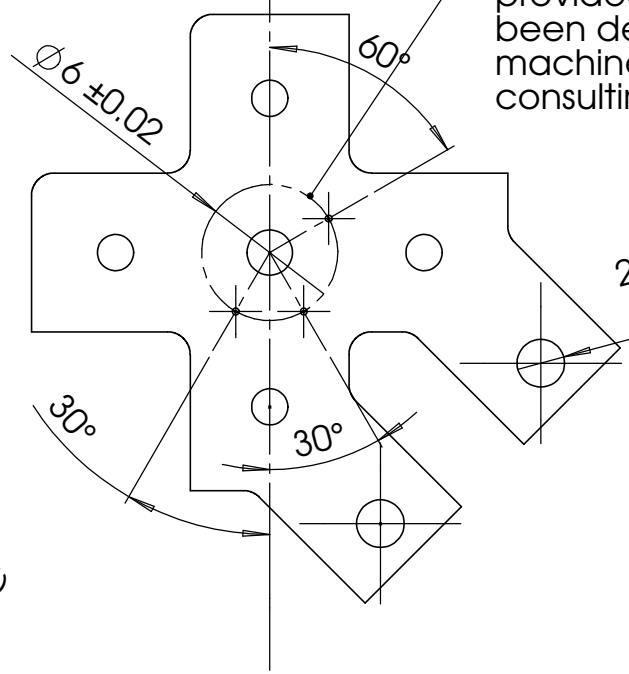

These three holes are clearance for wire. Dimension to be provided once the wire has been delivered, please do not machine these without consulting Sarah!

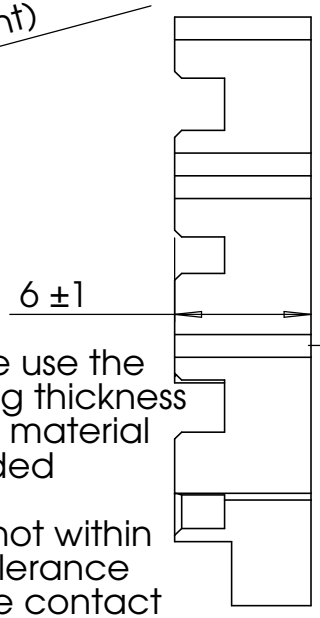

Please use the existing thickness of the material provided

If it is not within this tolerance please contact Sarah

If anything is at all unclear, or any tolerances cannot be met, please contact Sarah before proceeding
sarah.woodrow@physics.ox.ac.uk
Ext 72265

UNLESS OTHERWISE SPECIFIED: DIMENSIONS ARE IN MILLIMETERS SURFACE FINISH: TOLERANCES: LINEAR: ANGULAR:	FINISH:	DEBUR AND BREAK SHARP EDGES	DO NOT SCALE DRAWING / REVISION

	NAME	SIGNATURE	DATE
DRAWN			
CHK'D			
APPV'D			
MFG			
Q.A			

MATERIAL:

WEIGHT:

TITLE:

Ion trap - Macor holders Outer dims & holes

DWG NO. Ion trap - holder 1

A4

SCALE:3:1

SHEET 1 OF 1

NB the slots are symmetric, so these dimensions & tolerances apply in all 4 symmetric locations

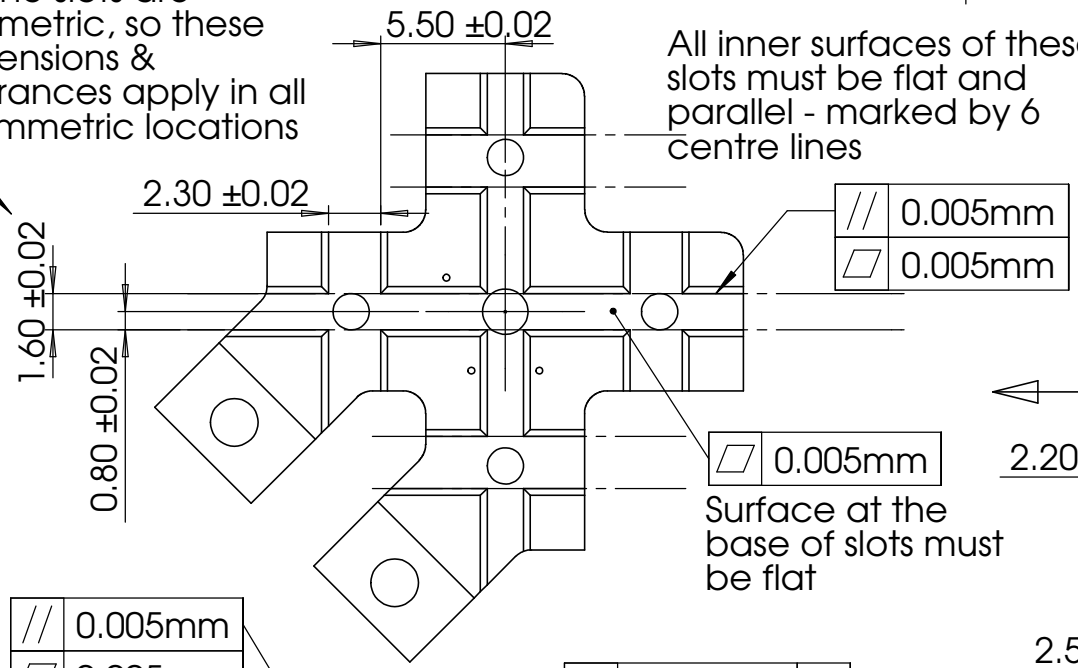

All inner surfaces of these slots must be flat and parallel - marked by 6 centre lines

Surface at the base of slots must be flat

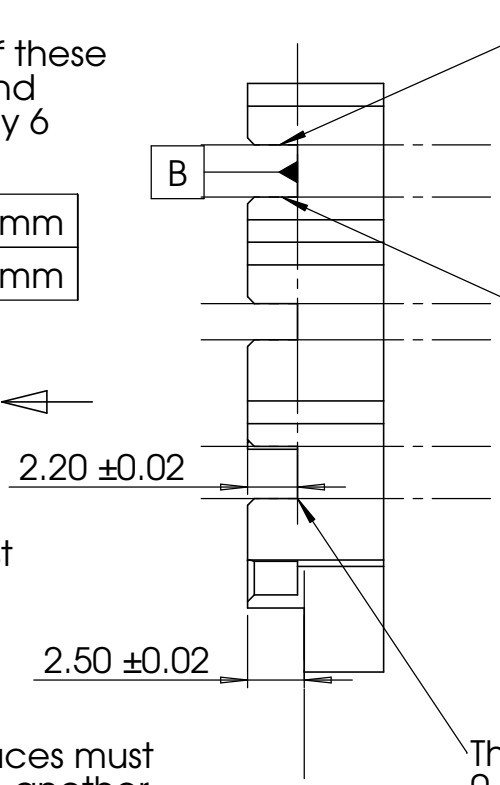

// 0.005mm
▱ 0.005mm

Slot walls must be flat and parallel - marked by 6 centre lines

⊥ 0.005mm | A | B

Walls must be perpendicular to the slot profile lines (A) and slot base surfaces (B)

i.e slot cross section should be rectangular, and normal to the slot cut direction, to within 5 microns

There can be a round of up to 0.05mm in the corners at the base of the slots (there is a chamfer on the mating pieces to allow for this)- but the bottom & side surfaces must be flat to within 5 microns aside from this

// 0.005mm
▱ 0.005mm

All inner surfaces of these slots must be flat and parallel - marked by 6 centre lines

⊥ 0.005mm | A

The intersecting slot surfaces must be perpendicular to one another

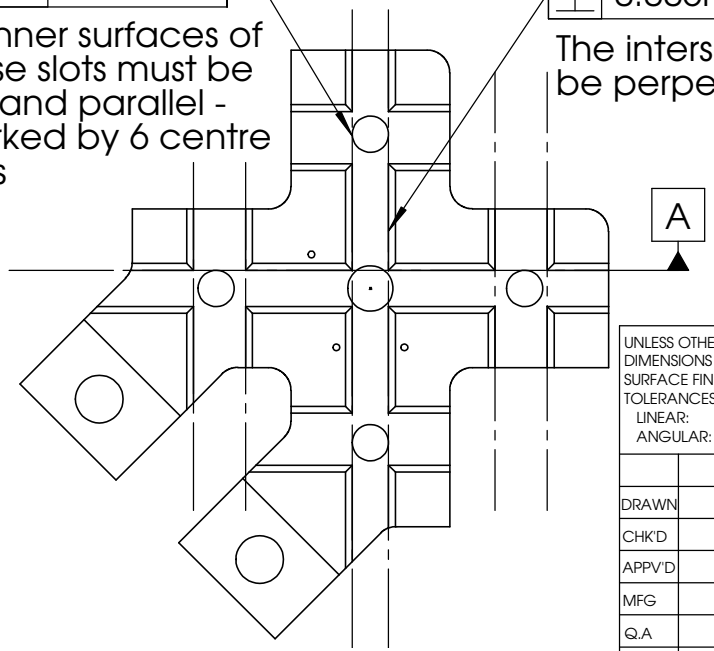

If anything is at all unclear, or any tolerances cannot be met, please contact Sarah before proceeding
sarah.woodrow@physics.ox.ac.uk
Ext 72265

UNLESS OTHERWISE SPECIFIED: DIMENSIONS ARE IN MILLIMETERS SURFACE FINISH: TOLERANCES: LINEAR: ANGULAR:	FINISH:	DEBUR AND BREAK SHARP EDGES

	NAME	SIGNATURE	DATE
DRAWN			
CHK'D			
APPV'D			
MFG			
Q.A			

MATERIAL:

WEIGHT:

DO NOT SCALE DRAWING | REVISION

TITLE:

Ion trap - Macor holders Slot dimensions

DWG NO. Ion trap - holder 2 A4

SCALE:3:1 | SHEET 1 OF 1